

**Manuscript version: Author's Accepted Manuscript**

The version presented in WRAP is the author's accepted manuscript and may differ from the published version or Version of Record.

**Persistent WRAP URL:**

<http://wrap.warwick.ac.uk/161908>

**How to cite:**

Please refer to published version for the most recent bibliographic citation information. If a published version is known of, the repository item page linked to above, will contain details on accessing it.

**Copyright and reuse:**

The Warwick Research Archive Portal (WRAP) makes this work by researchers of the University of Warwick available open access under the following conditions.

© 2022 Elsevier. Licensed under the Creative Commons Attribution-NonCommercial-NoDerivatives 4.0 International <http://creativecommons.org/licenses/by-nc-nd/4.0/>.



**Publisher's statement:**

Please refer to the repository item page, publisher's statement section, for further information.

For more information, please contact the WRAP Team at: [wrap@warwick.ac.uk](mailto:wrap@warwick.ac.uk).

# A coupled conjugate heat transfer and CFD model for the thermal runaway evolution and jet fire of 18650 lithium-ion battery under thermal abuse

Depeng Kong<sup>a,c\*</sup>, Gongquan Wang<sup>a</sup>, Ping Ping<sup>b</sup>, Jenifer Wen<sup>c,\*</sup>

<sup>a</sup> Center for Offshore Engineering and Safety Technology, China University of Petroleum (East China), Qingdao 266580, P R China

P R China

<sup>b</sup> College of Chemical Engineering, China University of Petroleum (East China), Qingdao 266580, P R China

<sup>c</sup> Warwick FIRE, School of Engineering, University of Warwick, Library Road, Coventry CV4 7AL, UK

**Abstract:** Thermal runaway (TR) is a major safety concern for lithium-ion batteries. A TR model incorporating the resulting jet fire can aid the design optimization of battery modules. A numerical model has been developed by coupling conjugate heat transfer with computational fluid dynamics (CFD) to capture the cell temperature and internal pressure evolution under thermal abuse, venting and subsequent combustion of 18650 lithium-ion batteries. The lumped model was employed to predict the thermal abuse reactions and jet dynamics, while the vented gas flow and combustion were solved numerically. Model validation has been conducted with newly conducted experimental measurements for the transient flame height of jet fire and temperatures at selected monitoring points on the cell surface and above the cell. The validated model was then used to investigate the effect of the SOCs on the evolution of TR and subsequent jet fires. Increasing SOCs shortens the onset time of TR and enlarges the peak jet velocity. The peak heat release rates and flame height of the jet fire increase with the increase of the SOC. The developed modelling approach extends the TR model to jet fire. It can potentially be applied to assist the design of battery modules.

**Keywords:** Lithium-ion battery; Thermal runaway; Cell venting; Jet fire; Numerical simulation

## Nomenclature

\* Corresponding author. E-mail address: [kongdepeng@upc.edu.cn](mailto:kongdepeng@upc.edu.cn) (D. Kong); [Jennifer.Wen@warwick.ac.uk](mailto:Jennifer.Wen@warwick.ac.uk) (J. X. Wen)

$A$	frequency factor ( $\text{s}^{-1}$ )	$Y$	mass fraction (-)
$A_v$	vent area of cell ( $\text{m}^2$ )		
$A_s$	Sutherland coefficient ( $\text{kg m}^{-1} \text{s}^{-1} \text{K}^{-1/2}$ )		Greek symbols
$C_d$	discharge coefficient at Level 2 (-)	$\alpha$	fractional degree of conversion (-)
$C_D$	discharge coefficient at Level 3 (-)	$\gamma$	heat capacity ratio (-)
$C_p$	heat capacity at constant pressure ( $\text{J kg}^{-1} \text{K}^{-1}$ )	$\varepsilon$	eddy dissipation rate ( $\text{W kg}^{-1}$ )
$C_v$	heat capacity at constant volume ( $\text{J kg}^{-1} \text{K}^{-1}$ )	$\varepsilon_{\text{cell}}$	surface emissivity (-)
$C_{\varepsilon 1}, C_{\varepsilon 2}, C_{\mu}$	Model constants used in turbulence model (-)	$\kappa$	thermal conductivity ( $\text{W m}^{-1} \text{K}^{-1}$ )
$D$	diffusion coefficient ( $\text{m}^2 \text{s}^{-1}$ )	$\nu$	viscosity ( $\text{m}^2 \text{s}^{-1}$ )
$Ea$	activation energy ( $\text{J mol}^{-1}$ )	$\rho$	density ( $\text{kg m}^{-3}$ )
$g$	gravitational acceleration ( $\text{m s}^{-2}$ )	$\sigma$	Stefan-Boltzmann constant ( $\text{W m}^{-2} \text{K}^{-4}$ )
$h$	sensible enthalpy ( $\text{J kg}^{-1}$ )	$\sigma_k, \sigma_\varepsilon$	Prandtl numbers for $k$ and $\varepsilon$ (-)
$h_{\text{cell}}$	convective heat transfer coefficient ( $\text{W m}^{-2} \text{K}^{-1}$ )	$\varphi$	mass fraction in the vent gas mixture (-)
$H$	heat release per unit mass ( $\text{J kg}^{-1}$ )	$\omega$	reaction rate of the gas species ( $\text{kg m}^{-3} \text{s}^{-1}$ )
$k$	turbulent kinetic energy ( $\text{J kg}^{-1}$ )		
$m$	mass ( $\text{kg}$ )		Subscript
$\dot{m}$	mass flow rate ( $\text{kg s}^{-1}$ )	0	initial value
$M$	molar mass ( $\text{kg mol}^{-1}$ )	1, cell	parameters inside the cell (Level 1)
$Ma$	Mach number (-)	2	parameters at the orifice (Level 2)
$n$	number of moles (mol)	3	parameters after a notional expansion to ambient conditions (Level 3)
$P$	pressure (Pa)	a	ambient
$Pr$	Prandtl number (-)	c	cathode decomposition
$q$	reaction heat from combustion ( $\text{W m}^{-3}$ )	DMC	parameters for electrolyte vapor
$Q$	reaction heat inside cells ( $\text{W m}^{-3}$ )	e	electrolyte decomposition
$R$	gas constant ( $\text{J K}^{-1} \text{mol}^{-1}$ )	ec	electrochemical reactions
$T$	temperature (K)	gas	parameters for generated gases
$T_s$	Sutherland coefficient (K)	PVDF	binder reaction
$u$	ambient air velocity ( $\text{m s}^{-1}$ )	SEI	SEI decomposition
$V_h$	headspace volume ( $\text{m}^3$ )	t	turbulence
$W$	generated gases moles per fractional degree (mol)		

## 1. Introduction

To combat global climate change and achieve carbon neutrality, worldwide governments have been vigorously pushing for the electrification of transport and energy storage systems (ESS). This stimulated rapid development of battery technologies, resulting in the explosive growth of electric vehicles (EVs) [1].

With relatively high energy density, extended cycle lifespan and trivial environmental pollution [2], abundant lithium-ion batteries (LIBs) have flooded the EV market as EV power sources and ESS. However, the recent proliferating fire and explosion accidents caused by thermal runaway (TR) of LIBs have raised increasing public concern and issued a warning sign about the urgent need to improve LIB safety [3].

As LIBs for hybrid electric vehicles and battery electric vehicles are typically in the order of 10-100 kW or MW or even higher scale, the LIB module in such applications usually consists of hundreds to thousands cells [4]. TR of one single cell usually generates excessive heat and flammable gases including H<sub>2</sub>, CH<sub>4</sub>, C<sub>2</sub>H<sub>4</sub>, C<sub>2</sub>H<sub>6</sub>, CO and other hydrocarbons [5-10]. The heat release from their combustion as well as the heat generation inside the cell can easily heat up the adjacent cells, resulting in TR propagation to the neighboring cells and the failure of the whole LIB module. For reliable prediction of the probability of a propagating failure as well as safe design to mitigate TR propagation in LIB module, accurate models are required to simulate the heat transfer between cells. TR propagation can generally be attributed to all three models of heat transfer, including conduction, convection, and radiation. TR propagation dominated by heat conduction across solid materials have been extensively modelled [11-14]. Heat convection through the fluid medium between the cells, such as melting phase change materials and coolant, can also result TR propagation from cell to cell inside a LIB module and studied in [15-18]. In comparison, the effect of convection and radiation from flame on TR propagation was rarely investigated despite its significant importance. Stoliarov et al. [19-21] firstly quantified internal heat generation and heat release associated with flaming combustion of vented materials, employing a novel copper slug battery calorimetry. Their works [19-21] also revealed combustion heat was more than the sum released heat from chemical reactions and the electric energy of short circuit during TR, alarming the subsequent researches should pay more attention to the thermal hazard from combustion during TR of LIBs. Liu et al [22] estimated the combustion heat release of a 243 Ah

LiFePO<sub>4</sub>/graphite LIB cell, and the peak heat release rate (HRR) and total heat release was observed as high as 88.6 kW and 19530.6 kJ. They also pointed out that the flaming combustion accelerated the TR progress. The calorimetry results from other researchers [23-27] also indicated that the contribution of the heat generated from the combustion of the ejected materials to TR propagation could not be neglected. It is hence important to include the combustion of venting gases in TR models to obtain more realistic heat transfer between the failure and surrounding cells in the LIB module.

The combustion chemistry of the ejected materials has been addressed in some published studies to assess the thermal hazards [9, 28, 29]. Johnsplash et al. [28] employed the Cantera 2.3.0 code with GRI-Mech 3.0 mechanism to simulate the combustion of three different kinds of abused LIBs in air. Fernandes et al. [9] also investigated combustion properties of the released gases in the Chemical Workbench Code and CHEMKIN-II. In addition to the analysis of the combustion chemistry, Larsson et al. [29] used a propane fire source to substitute jet fire of LIBs to evaluate effects of combustion on cell-to-cell propagation. Despite such progress, coupled numerical studies of the TR process, ejection dynamics and combustion have not been reported. Although several TR models of LIBs [30-34] have been proposed to investigate the evolution of temperature and voltage, the venting and jet fire events were not addressed.

The bottleneck of the modeling development of ejection flow and combustion of LIBs during TR lies in the complexity in the underlying electrothermal reactions inside LIBs as well as the highly transient flow field outside LIBs. The heat and gases generated through the electrothermal reactions inside LIBs result in pressure build-up within the cell and eventually trigger the opening of the safety valve to activate the venting. The venting phenomenon directly affects external flow and combustion characteristics of LIBs. Previous attempts to couple the internal and external events can be categorized into two approaches. The first approach is based on using zero dimensional (0D) lumped model to predict thermal reaction and jet flow parameters.

Coman et al. [35] included venting of the electrolyte and contents of the jelly roll in a lumped model for TR coupling thermal and flow equations. They quantified the energy flowing out the cell with the ejecta to capture the cooling effect of the safety valve opening. The model was later extended to address the temperature-pressure evolution and gas generation within the cell with the pressure relief mechanism expressed by isentropic flow equations [36]. The subsequent venting models mostly [37, 38] followed the model frame of Coman [35, 36]. Ostank et al. [37] simulated onset and evolution of LIB TR using a coupled thermal and venting lumped model, and the flow parameter through the vent was modeled by compressible flow equations after vent opening. Bugryniec et al. [39] proposed an abuse model to investigate cell pressurization and simmering reactions of LIBs, and achieved similar prediction of the pressure accumulation in comparison with a classical TR model [35, 36]. Mao et al. [38] developed a lumped model for the characteristics of the 18650-type LIB jet flow and fire dynamics. The flame height was predicted combining using some correlations based on the flame Froude number. Although such modeling efforts have successfully described the interconnection between the thermal abuse reactions, pressure build-up and venting characteristics, the subsequent flow field following venting and the evolution of the resulting jet fire were not addressed. Kim et al. [40] developed an alternative approach by considering the random porous media rather than classical solid to model the LIBs. They used the change of the porous media scaling factor at the bottom of the vent to link cell interior and exterior. Though this model could predict cell venting and gas-phase reactions well, the prediction of heat flux through the cell surface and the corresponding temperature evolution inside the cell was unrealistic owing to the absence of accurate estimation for the convective boundary conditions [41], compared with the conjugate heat transfer calculation based on fluid-solid coupling widely employed in some published works [16, 18, 32]. Thus, it would be problematic to extend this approach from a single cell to groups of cells and modules to achieve the prediction of TR

propagation.

A single cell TR model incorporating the resulting jet fire is necessary to facilitate the predictions of TR propagations. The previous models have failed to achieve reliable predictions of realistic distribution and evolution of temperatures on the cell surfaces and the surrounding fluid during single cell TR and jet fire. Closing this knowledge gap is indeed a key objective of the present study, which is the first step toward developing propagation models considering effects of jet fire.

Aiming at accurately capturing the temperature and internal pressure evolution inside the cell as well as the venting/combustion behaviors during TR, a novel approach was proposed based on the coupled fluid-solid heat transfer, sub-models for TR evolution, internal pressure, the fluid dynamics during venting and combustion. The TR sub-model consists of the transient heat conduction equation and a series of electrochemistry reactions described by Arrhenius law, while the prediction of pressure and venting velocity was achieved by a lumped model in the form of several ordinary differential equations (ODEs). The gas flow and combustion reactions in the air zone were calculated by the Reynolds-averaged Navier-Stokes (RANS) approach with turbulent models and the eddy dissipation concept (EDC) for combustion. A dynamic boundary condition at the top of the vent was employed to couple the TR process inside LIBs and characteristic external flow field. The numerical model was established for 18650 cells with NCA cathode and implemented within the frame of open source computational fluid dynamics (CFD) code OpenFOAM. Validation was carried out by comparing the predictions and measurements for cell surface temperature and flame heights. The validated model was then used to investigate the effects of states of charge (SOCs) on the transient temperature, cell internal pressure, venting and jet fire.

## 2. Model framework

**Fig. 1** illustrates the thermal behaviors and mechanism of the cell under thermal abuse. This process is coupled by the temperature increase and the internal pressure evolution. A series of exothermic reactions and electrochemical reactions take place leading to continued temperature rise and pressure accumulation under elevated temperatures [42, 43]. The solid electrolyte interface (SEI) layer, formed on the graphite anode due to the irreversible electrochemical decomposition of electrolyte, may decompose firstly at about 69 °C [44]. Then the electrolyte reacts with the anode when the temperature reaches around 120 °C [45]. The cathode and anode contact together and the internal short circuit will occur once the separator shrinks at about 130 °C [46]. Then the exothermic decomposition reactions will occur and release oxygen at different temperature for various cathode materials, the onset temperature of which is around 160 °C [47] for  $\text{LiNi}_{0.8}\text{Co}_{0.15}\text{Al}_{0.05}\text{O}_2$  (NCA) cathode studied in this work. When the temperature exceeds about 200 °C, the electrolyte will also decompose exothermically itself [48]. Finally, the binder used for maintaining integrity of the electrodes will react with the cathode material and  $\text{Li}_x\text{C}_6$  after 260 °C [42, 43]. In addition to heat generation, the above electrochemical reactions also release gases, which together with the evaporation of electrolyte leads to pressure accumulation inside the cell [36]. During the course of the above reactions, the vent valve will open at the designed pressure, leading to the initial venting event. As thermal abuse develops, once the heat generated is more than what can be dissipated, the above processes eventually lead to TR as well as the second time gas ejection [43, 49]. The flammable gaseous mixture of electrolyte vapors and generated gases may be ignited by the ejected hot materials such as melting current collector, resulting in a jet fire.

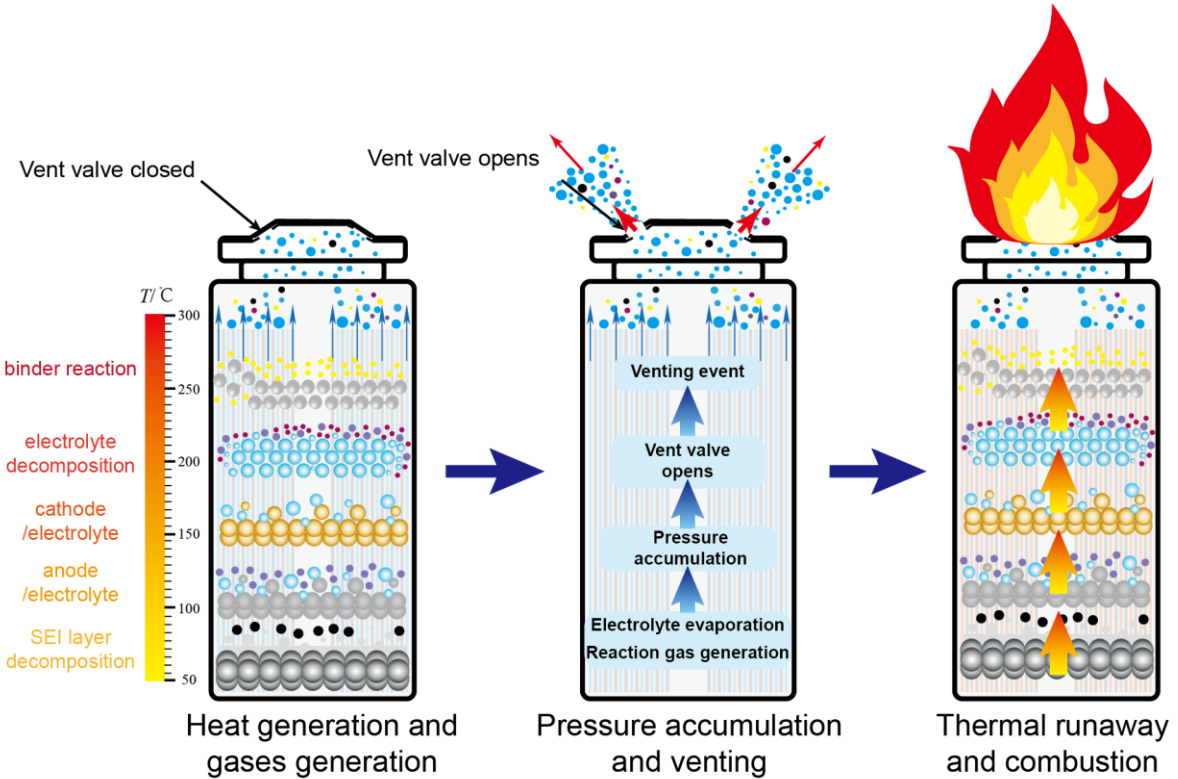


**Fig. 1.** Schematic of mechanism of the venting, combustion and thermal runaway for the NCA cell under thermal abuse.

By analyzing the venting, combustion and TR of the NCA cell under thermal abuse, a numerical model was developed and implemented in OpenFOAM to capture the temperature and internal pressure evolution inside the cell as well as the venting and combustion behaviors during TR. The flow chart of the TR model is shown in **Fig. 2**, some key steps in TR sub-model essentially follow that of our previously developed electro-thermal model [32, 50] and includes several steps: (1) creating the geometry and mesh, and also defining the initial conditions; (2) calculating the fractional degree of conversion and reaction heat, solving energy equation in the cell zone as to be described in Sections 2.1 Thermal runaway sub-model; (3) solving internal pressure and venting model, and calculating related kinetic parameters to be discussed in Sections 2.2 Pressure and venting sub-model; (4) using calculated kinetic parameters as dynamic boundary conditions to couple the cell and air zones; (5) solving a series of conservation equations for mass, momentum, species and energy; (6) repeating the above steps until the set end time of calculation; (7) checking whether the

predictions are in agreements with the measurements. If not, revising the model parameters and recalculating.

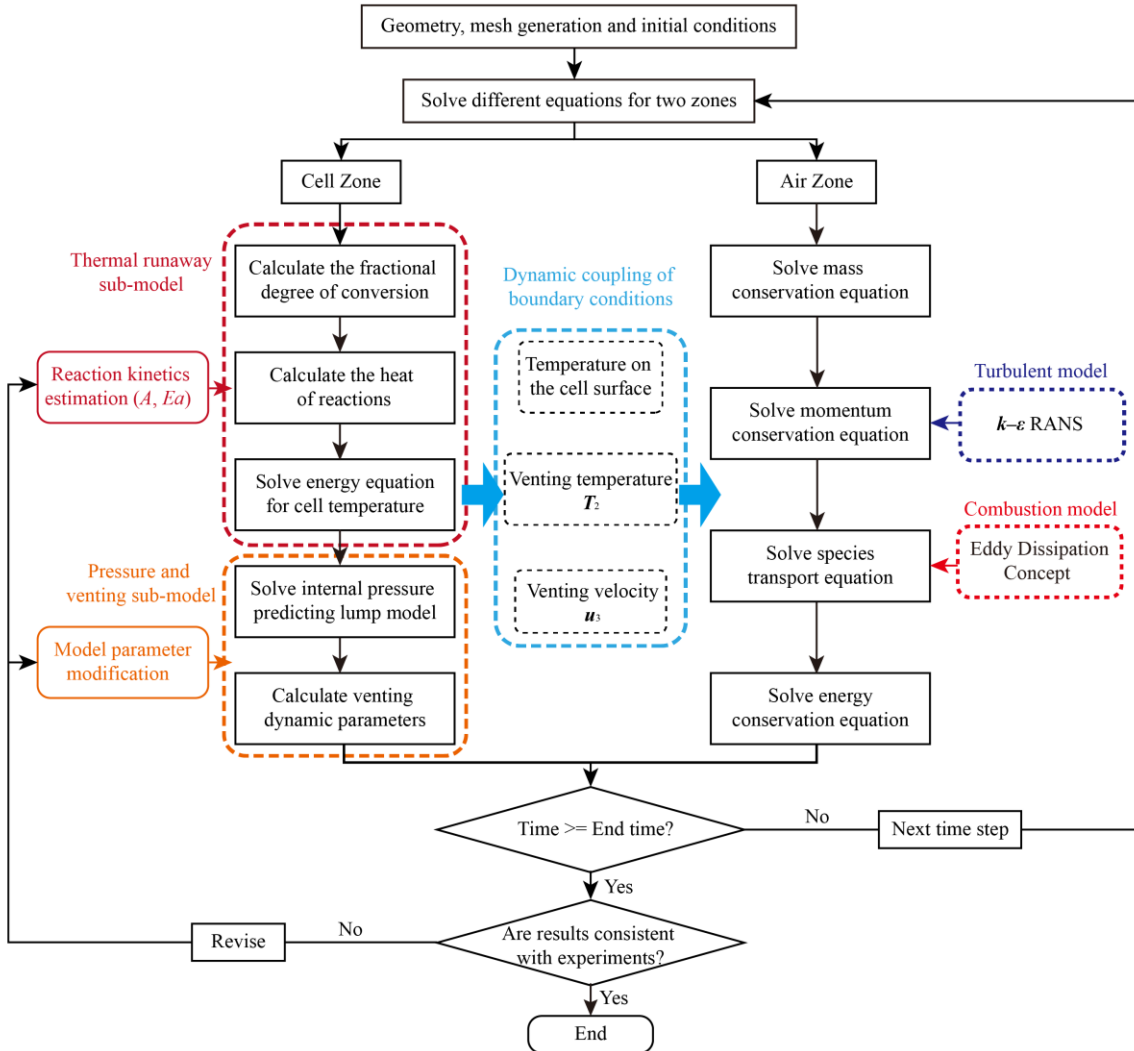


**Fig. 2.** Flow chart of the thermal runaway model.

## 2.1 Thermal runaway sub-model

### 2.1.1 Thermal conservation equations

In the cell porous jellyroll, the convective heat transfer from the flow of the evaporated electrolyte and the generated gases is negligible and the thermal conduction dominates internal heat transport in the cell, thus the TR model is developed based on the heat conduction in solids, which can be described by:

$$\rho C_p \frac{\partial T}{\partial t} = \nabla \cdot (\kappa \nabla T) + \sum \dot{Q}_i \quad (1)$$

$$\dot{Q}_{rec} = \sum \dot{Q}_i = Q_{SEI} + Q_a + Q_c + Q_{ee} + Q_e + Q_{PVDF} \quad (2)$$

where  $\rho$  is the density;  $T$  is the temperature;  $C_p$  is the heat capacity;  $\kappa$  is the thermal conductivity;  $\dot{Q}_i$  is the heat source of the thermal reactions. In theory,  $\dot{Q}_{rec}$  consists of  $Q_{SEI}$ ,  $Q_a$ ,  $Q_c$ ,  $Q_{ee}$ ,  $Q_e$  and  $Q_{PVDF}$ , corresponding to the heat from decomposition of the SEI layer, reaction between anode and electrolyte, internal short circuit, reaction between cathode and electrolyte, decomposition of electrolyte and binder reaction respectively [50]. But considering the effect of various lithiated states on the heat and kinetic parameters of cell materials, the whole thermal decomposition process for the cells with various SOC is divided into six stages by different temperature ranges, according to the temperature rise curve measured by the accelerating rate calorimeter (ARC), aiming at obtaining optimal thermal kinetic parameters. For each thermal reaction at various stages, the heat generation can be determined as:

$$\dot{Q}_i = H_i \frac{d\alpha_i}{dt} \quad (3)$$

where  $H_i$  is the enthalpy of one of the specific thermal reactions ( $J \text{ m}^{-3}$ ),  $\alpha_i$  is the fractional degree of conversion of various stage thermal reactions. The reaction conversion rate for various stages can be calculated by following the Arrhenius law:

$$\frac{d\alpha_i}{dt} = A_i \alpha_i \exp\left(-\frac{Ea_i}{RT}\right) \quad (4)$$

where  $A_i$  is the frequency factor;  $Ea_i$  is the activation energy;  $R$  is molar gas constant with the value of  $8.314 \text{ J mol}^{-1} \text{ K}^{-1}$ ; The following kinetic analysis of temperature data is then used to obtain the parameters for various reaction stages.

### 2.1.2 Estimation of reactions kinetics

Assuming the cell is heated under adiabatic condition, the heat generated within the system will just heat the system itself without any heat loss to the surrounding. The energy conservation equation of the cell under adiabatic condition can be expressed as:

$$\rho C_p \frac{dT}{dt} = H_i \frac{d\alpha_i}{dt} \quad (5)$$

For one reaction stage  $i$ , the initial  $T_{0,i}$  and maximum temperature  $T_{\max,i}$  can then be obtained. The heat generation during this stage can be calculated as:

$$H_i = \rho C_p (T_{\max,i} - T_{0,i}) \quad (6)$$

Integrate the Eq.(5) over time, then the following equation can be given:

$$\rho C_p (T - T_{0,i}) = H_i \alpha_i \quad (7)$$

The fractional degree of conversion for reaction stage  $i$  at any time  $\alpha_i$  can be given by substituting Eq. (6) into Eq.(7):

$$\alpha_i = \frac{T - T_{0,i}}{T_{\max,i} - T_{0,i}} \quad (8)$$

Considering the effect of various lithiated states on the heat and kinetic parameters of cell materials, the optimal thermal kinetic parameters were calculated by the temperature rise curve measured at adiabatic condition from Golubkov et al [51]. As shown in Fig. 3 (a) and (b), the whole thermal decomposition process was divided into six stages according to the temperature rise rate range and each stage was linearly fitted individually. For a certain stage, the temperature rise rate considered as the first order reaction can be calculated as [32]:

$$\frac{dT}{dt} = (T_{\max,i} - T_{0,i}) A_i \exp\left(-\frac{Ea_i}{RT}\right) \alpha_i \quad (9)$$

Then the equation from Eq.(9) taken logarithms can be employed to obtain the thermal kinetic parameters, and the detailed derivation process can be found in reference [32].

$$\ln\left(\frac{dT/dt}{T - T_{0,i}}\right) = \ln A_i - \frac{Ea_i}{R} \cdot \frac{1}{T} \quad (10)$$

The parameters  $A_i$ ,  $Ea_i$  can be determined from the slope and interception of the linear fitting curve of  $\ln((dT/dt)/(T-T_{0,i}))$  versus  $-1/T$ , and a calculation case for reaction stage IV of the cell with 75% SOC is shown in Fig. 3 (b). The mean square residual for the linear fitting of various stages were higher than 0.9, indicating

the divisions and fitting were reasonable. All the kinetic and thermodynamic parameters used for 25%, 50% and 75% SOC in this study are summarized in **Table 1**.

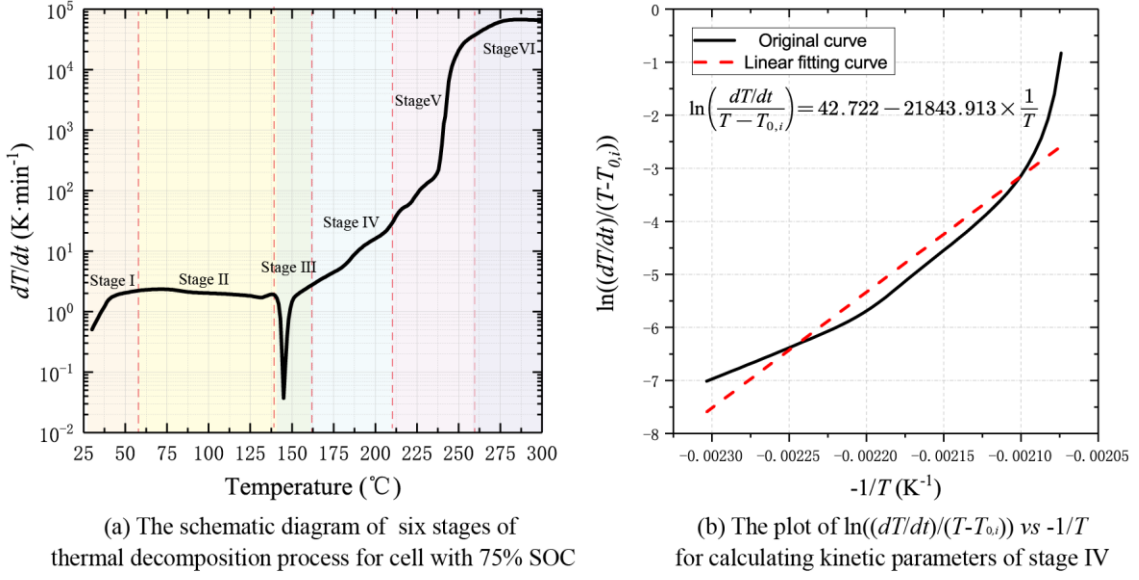


**Fig. 3.** The temperature range division and fitting process used for calculating kinetic parameters from Golubkov's data [51].

**Table 1**

Kinetic and thermodynamic parameters used in the model.

SOC	Stage	$T_{0,i}$ (°C)	$H_i$ (J m <sup>-3</sup> )	$Ea_i$ (J mol <sup>-1</sup> )	$A_i$ (s <sup>-1</sup> )
25%	II	84	$7.94 \times 10^7$	$3.66 \times 10^4$	45.50
	III	117	$9.62 \times 10^7$	$1.00 \times 10^5$	$1.49 \times 10^9$
	IV	157	$2.64 \times 10^7$	$3.80 \times 10^5$	$3.22 \times 10^{35}$
	V	168	$1.01 \times 10^8$	$2.04 \times 10^5$	$5.66 \times 10^{19}$
	VI	210	$1.20 \times 10^9$	$2.15 \times 10^5$	$2.80 \times 10^{20}$
	II	69	$1.23 \times 10^8$	$3.60 \times 10^4$	50.48
50%	III	120	$9.62 \times 10^7$	$3.53 \times 10^5$	$1.60 \times 10^{40}$
	IV	160	$1.20 \times 10^8$	$2.54 \times 10^5$	$5.21 \times 10^{24}$
	V	210	$1.20 \times 10^8$	$2.02 \times 10^5$	$5.65 \times 10^{19}$
	VI	260	$1.07 \times 10^9$	$2.16 \times 10^5$	$2.75 \times 10^{20}$
75%	II	69	$1.81 \times 10^8$	$3.58 \times 10^4$	55.47
	III	144	$3.85 \times 10^7$	$5.85 \times 10^5$	$1.98 \times 10^{69}$
	IV	160	$1.20 \times 10^8$	$1.73 \times 10^5$	$3.58 \times 10^{18}$
	V	210	$1.20 \times 10^8$	$4.66 \times 10^5$	$8.57 \times 10^{49}$
	VI	260	$1.08 \times 10^9$	$3.73 \times 10^5$	$2.36 \times 10^{40}$

## 2.2 Pressure and venting sub-model

During TR, the pressure inside the cell will accumulate due to the evaporation of electrolyte and gas generation until the vent valve is breached. When the temperature rises to the ignition point or an ignition source such as spark appears, the combustible gas mixture will be ignited and results in the jet fire. The fluid dynamic parameters of the external flow around the vent valve directly affects the LIB jet fire behaviors, thus the accurate prediction of the internal pressure and venting behavior of LIBs is the cornerstone of modeling LIB jet fire.

The flow chart of the internal pressure and venting sub-model is shown in **Fig. 4**. The key steps include:

- (1) Check whether the internal cell pressure has exceeded the vent pressure. If this condition is true, the vent valve will open.
- (2) Check whether the vent valve has opened. If false, the state equation in the Section **2.2.1** Pressure accumulation before venting will be employed to calculate the partial pressure of electrolyte vapor and generated gases.
- (3) Otherwise, then check a relation between the internal pressure and ambient pressure to determine whether the flow is subsonic or choked.
- (4) Calculate dynamic parameters according to two different flow states from an isentropic nozzle flow in the Section **2.2.3** Dynamical process of flowing through the vent valve.
- (5) Solve ODEs in the Section **2.2.2** Dynamic change of pressure during venting for the partial pressure of electrolyte vapor and generated gases.
- (6) Calculate the internal pressure within the cell, and output some dynamic parameters to the combustion model as boundary conditions.
- (7) Repeating the above steps until the set end time of calculation.

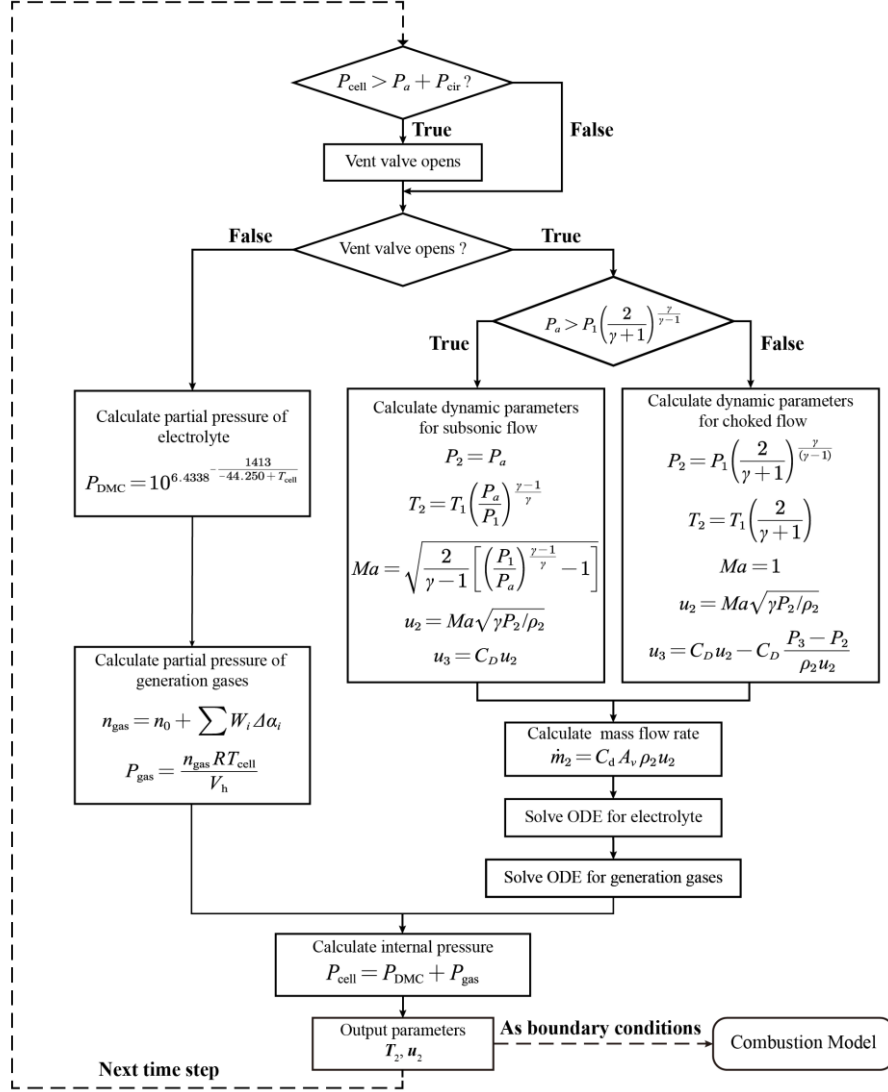


**Fig. 4.** Flow chart of the internal pressure and venting sub-model.

### 2.2.1 Pressure accumulation before venting

The pressure accumulation before venting mainly considers contributions the evaporation of the electrolyte under thermal abuse condition and gas generation from the decomposition reactions [36]. Thus, the internal cell pressure at any time before venting under thermal abuse condition can be calculated by Dalton's law:

$$P_{\text{cell}} = P_{\text{DMC}} + P_{\text{gas}} \quad (11)$$

where  $P_{\text{DMC}}$  is the partial pressure of electrolyte vapor and  $P_{\text{gas}}$  is the partial pressure of the generated gaseous mixture. In the early stage of thermal abuse, the cell safety valve was closed, the electrolyte vapor and

generated gases remain inside the cell. As the cell temperature increases, the liquid electrolyte will evaporate and eventually reach vapor liquid equilibrium (VLE) conditions. ~~In this instance, the partial pressure of the electrolyte vapor is equal to its saturation pressure which increases with the increase of the temperature.~~ The saturation pressure can be expressed using Antoine's equation with the fitting coefficients of DMC electrolyte to calculate the partial pressure of electrolyte vapor [52]:

$$P_{\text{DMC}} = 10^{6.4338 - \frac{1413}{-44.250 + T_{\text{cell}}}} \quad (12)$$

where  $T_{\text{cell}}$  is the average temperature inside the cell. The valid temperature scope of Eq.(12) is 0 °C to 274 °C [52], which is effective to approximate the partial pressure of electrolyte vapor before the venting event. For the generated gaseous mixture in a sealed container before the vent event, the partial pressure is calculated using the state equation for ideal gas:

$$P_{\text{gas}} = \frac{n_{\text{gas}} RT_{\text{cell}}}{V_h} \quad (13)$$

~~where  $V_h$  is the headspace volume occupied by the vapor and gas, and  $n_{\text{gas}}$  is the total moles of the generated gases.  $n_{\text{gas}}$  can be calculated as follow from the conversion degree of thermal decomposition reactions that generate specific gases:~~

$$n_{\text{gas}} = n_0 + \sum W_i \Delta \alpha_i \quad (14)$$

where  $V_h$  is the headspace volume occupied by the vapor and gas, and  $n_{\text{gas}}$  is the total moles of the generated gases.  $n_0$  is the initial gas mole in the cell headspace volume,  $W_i$  is the moles of the generated gaseous mixture of reaction stage- $i$  at its equilibrium composition measured in the experiment. The generated gases were assumed to include H<sub>2</sub>, CO<sub>2</sub>, CO, CH<sub>4</sub>, C<sub>2</sub>H<sub>4</sub>, C<sub>2</sub>H<sub>6</sub> and O<sub>2</sub> according to the experimental results from Golubkov et al. [51].

The generation mechanism of hydrogen may be attributed to the reactions between Li and binders, the water-gas shift reaction and the oxidation of exposed Li with water [51, 53]. In this model, the reactions

between polyvinylidene fluoride (PVDF) and Li exposed in the surrounding electrolyte is mainly considered when the temperature is above 260 °C. When the temperature rises to about 100 °C, the SEI layer consisting of metastable components may decompose in thermally driven reactions and generate carbon dioxide [45]. In addition to the decomposition of SEI layer, the oxygen released might react with the electrolyte solvent to generate carbon dioxide [45]. In order to simplify the modeling, the generation of carbon dioxide is assumed to be entirely from the decomposition of DMC, which will occur when the temperature exceeds 200 °C [42]. The possible sources responsible for the release of carbon monoxide is the reduction of carbon dioxide with intercalated Li at the anode [53-55], thus this process is assumed to occur after the generation of carbon dioxide. The reduction of electrolyte by hydrogen to lithium carbonate is a possible generation process of methane [56-58], and this mechanism is considered after the generation of hydrogen. In addition to the SEI layer thermal decomposition [45], the reaction between lithium and SEI layer also contributes to the release of ethylene [59]. Ethane can be produced by the reactions of the solvent and lithium at the lithiated anode [45]. One possible source of oxygen release is from transiting of the delithiated  $\text{Li}_x(\text{Ni}_{0.80}\text{Co}_{0.15}\text{Al}_{0.05})\text{O}_2$  cathode material from layered to rock salt structure during the temperature from 175 °C to 600 °C [60, 61].

The detailed mechanism and corresponding chemical equations of above reactions are summarized in **Table S1**. Combined the analysis of the gas generation mechanism and the experimental data of Golubkov et al. [51], the calculated moles of the generated gases at various reaction stages  $W_i$  are summarized in **Table 2**.

**Table 2**

The generated gases moles of various reaction stages  $W_i$  (unit in mmol)

SOC (%)	$W_2$	$W_3$	$W_4$	$W_5$	$W_6$
25	5.025	-	-	22.325	61.908
50	5.024	0.628	37.950	123.873	27.475
75	7.161	1.085	53.575	139.965	69.874

## 2.2.2 Dynamic change of pressure during venting

The commercial LIBs generally consist of a pressure burst disk and a vent valve for safety purposes.

When the internal pressure of the cell increases to a critical pressure of  $P_{\text{cir}} = 1.9$  MPa for the currently considered 18650 cell [40], the vent valve opens to release the generated gases and aerosols of electrolyte vapor. Due to the breakdown of the VLE condition inside the cell, the previous equations of state under VLE condition is no longer valid and several ODEs can be written to simulate the dynamic change of the pressure with time inside the cell. Differentiating both sides of Eq.(11) with respect to time gives:

$$\frac{dP_{\text{cell}}}{dt} = \frac{dP_{\text{DMC}}}{dt} + \frac{dP_{\text{gas}}}{dt} \quad (15)$$

~~The above equation indicates the dynamic change of cell internal pressure during venting consists of the partial pressure change rate of electrolyte vapor and generated gases with time.~~ As for the partial pressure of the electrolyte vapor, the ideal gas law is used as the equation of state and then the derivative of both sides with respect to time is taken to give the differential form:

$$\frac{P_{\text{DMC}}}{M_{\text{DMC}}V_h} = \frac{m_{\text{DMC}}RT_{\text{cell}}}{M_{\text{DMC}}V_h} \quad (16)$$

$$\frac{dP_{\text{DMC}}}{dt} = \frac{RT_{\text{cell}}}{M_{\text{DMC}}V_h} \frac{dm_{\text{DMC}}}{dt} + \frac{m_{\text{DMC}}R}{M_{\text{DMC}}V_h} \frac{dT_{\text{cell}}}{dt} \quad (17)$$

where  $m_{\text{DMC}}$  is the mass of electrolyte vapor in the cell headspace, and  $M_{\text{DMC}}$  is the molar mass of DMC. ~~The two terms on the right hand side of Eq.(17) indicate the change of the partial pressure of electrolyte vapor is determined by the changes in the mass of electrolyte vapor in the headspace and the changes in cell average temperature.~~ The derivative of cell temperature with respect to time  $dT_{\text{cell}}/dt$  can be calculated from the energy equation in the cell zone, and the mass flow rate of DMC  $dm_{\text{DMC}}/dt$  through the vent valve can be expressed as follow:

$$\frac{dm_{\text{DMC}}}{dt} = -\varphi_{\text{DMC}}\dot{m}_2 \quad (18)$$

where  $\varphi_{\text{DMC}}$  is the mass fraction of DMC in the vent gas mixture.  $\dot{m}_2$  is the mass flow rate of the vent gas mixture through the orifice of vent valve, the detailed calculation of which will be investigated in the Section 2.2.3.

Similarly, the differential form of Eq.(13) is used to simulate the dynamic change of partial pressure of generated gases:

$$\frac{dP_{\text{gas}}}{dt} = \frac{RT_{\text{cell}}}{V_h} \frac{dn_{\text{gas}}}{dt} + \frac{n_{\text{gas}} R}{V_h} \frac{dT_{\text{cell}}}{dt} \quad (19)$$

~~The mole change rate of generated gases in the cell headspace is represented by the gas generation rate and the mole flow rate of gases through the vent valve:~~

$$\frac{dn_{\text{gas}}}{dt} = \sum W_i \frac{da_i}{dt} - \frac{\varphi_{\text{gas}} \dot{m}_2}{M_{\text{gas}}} \quad (20)$$

where the reaction rate of thermal decomposition  $da/dt$  can be calculated from the Eq(4).  $\varphi_{\text{gas}}$  is the mass fraction of generated gases in the vent gas mixture and  $M_{\text{gas}}$  is the average molar mass of generated gases mixture, calculated as  $\sum M_i n_i / \sum n_{\text{gas}}$ .

~~The parameters when the vent valve opens are employed as the initial condition of ODE, and the ODE is integrated in explicit Euler method to calculate the cell internal pressure  $P_{\text{cell}}$  considering effective arithmetic.~~

### 2.2.3 Dynamical process of flowing through the vent valve

One critical parameter to model the dynamic change of the cell internal pressure during venting is the mass flow rate through the vent valve. ~~After the vent valve opens, the dynamical process of gas flow can be regarded as an isentropic nozzle flow of the ideal gases, consisting of three level as shown in Fig. 5 [62, 63].~~ ~~the whole flow process consists of three levels: conditions inside the cell (Level 1), conditions at the orifice (Level 2) and conditions after a notional expansion to ambient conditions (Level 3)~~

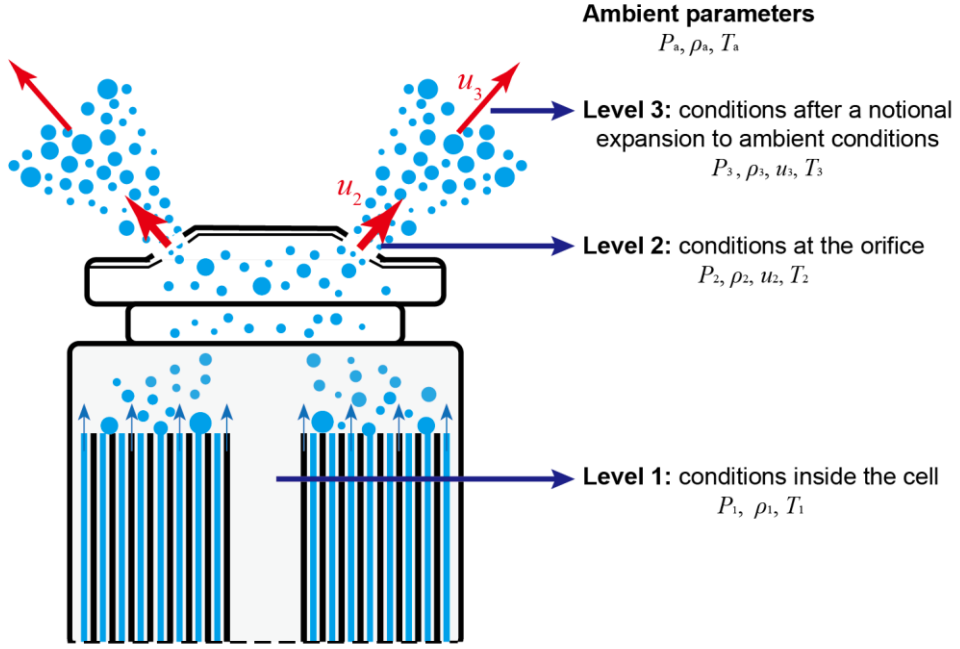


**Fig. 5.** Schematic of gas flow near the vent valve.

The parameters at Level 1 are equal to that inside the cell, and the flow parameters at Level 2 are calculated using a variant of the isentropic nozzle flow equations. In order to consider if the flow is subsonic or choked, the following conditional statement is first checked:

$$P_a > P_1 \left( \frac{2}{\gamma + 1} \right)^{\frac{\gamma}{\gamma - 1}} \quad (21)$$

where  $P_a$  is the ambient pressure and  $\gamma$  is the heat capacity ratio of venting gases. If the above inequality is true, the flow is subsonic, otherwise is choked. The pressure  $P_2$ , the temperature  $T_2$  at the orifice and the Mach number  $Ma$ , defined by the ratio of gas velocity  $u_2$  to the local speed of sound, are delimited by the type of flow. If the flow is subsonic [64]:

$$P_2 = P_a \quad (22)$$

$$T_2 = T_1 \left( \frac{P_a}{P_1} \right)^{\frac{\gamma - 1}{\gamma}} \quad (23)$$

$$Ma = \sqrt{\frac{2}{\gamma - 1} \left[ \left( \frac{P_1}{P_a} \right)^{\frac{\gamma - 1}{\gamma}} - 1 \right]} \quad (24)$$

As for the choked flow, the parameters are expressed with the Pseudo diameter approach [64]:

$$P_2 = P_1 \left( \frac{2}{\gamma + 1} \right)^{\frac{\gamma}{(\gamma - 1)}} \quad (25)$$

$$T_2 = T_1 \left( \frac{2}{\gamma + 1} \right) \quad (26)$$

$$Ma = 1 \quad (27)$$

The venting gas velocity  $u_2$  and the mass flow rate  $\dot{m}_2$  through the vent valve can be determined as [64]:

$$u_2 = Ma \sqrt{\gamma P_2 / \rho_2} \quad (28)$$

$$\dot{m}_2 = C_d A_v \rho_2 u_2 \quad (29)$$

where  $\rho_2$  is the gas density when the gas flows out from the orifice, calculated as  $P_2 M_{\text{gas}} / R T_2$ .  $A_v$  is the vent area of cell.  $C_d$  is a discharge coefficient considering a non-ideal effect of the irreversible process [65].

For the high-pressure gas venting from the cell, the under-expanded jet flow will expand into supersonic flow after leaving the nozzle. ~~The gas pressure will gradually decrease until that drops to ambient pressure while the gas velocity will progressively increase until that reaches the local speed of sound. Thus,~~ A simplified notional nozzle model substituting for the under-expanded jet flow should be employed to obtain the state parameters of the steady flow at Level 3 as well as provide an equivalent inlet condition for the following numerical simulation of jet fire. Birch et al. [62, 63] proposed a concept of “pseudo-diameter” to calculate the effective velocity  $u_3$  at Level 3:

$$u_3 = \begin{cases} C_D u_2, & \text{if subsonic flow} \\ C_D u_2 - C_D \frac{P_3 - P_2}{\rho_2 u_2}, & \text{if choked flow} \end{cases} \quad (30)$$

where  $P_3$  is equal to the ambient pressure  $P_a$ ,  $C_D$  is a volume discharge coefficient considering the a possible non-uniform velocity profile at the nozzle and the momentum loss when the melting solid particles flow through the vent valve [38]. ~~It is worth noting that the parameters at Level 3 only affect the behaviors of airflow field after venting as well as jet fire during TR, instead of the cell internal pressure and parameters at Level 2.~~ Finally,  $u_3$  will be used as the dynamic boundary condition of the velocity inlet, and  $T_2$  will be the

dynamic temperature boundary condition of the venting gas inlet, participating in the later numerical simulation in the air zone. The values of above-mentioned parameters in cell zone are listed in **Table 3**.

**Table 3**

Kinetic and thermodynamic parameters used in the model

Parameters	Value	Unit	Source
$A_v$	9.8	mm <sup>2</sup>	Ref.[37]
$C_d$	0.8	-	Ref.[65]
$C_D$	$3.3 \times 10^{-3}$	-	Fit
$C_p$	830	J kg <sup>-1</sup> K <sup>-1</sup>	Ref.[50]
$M_{DMC}$	90.08	g mol <sup>-1</sup>	Ref.[66]
$n_0$	$4.33 \times 10^{-5}$	mol	Fit
$P_a$	101325	Pa	Calc
$V_h$	1.158	cm <sup>3</sup>	Ref.[37]
$\gamma$	1.4	-	Ref.[38]
$\kappa$	3.4	W m <sup>-1</sup> K <sup>-1</sup>	Ref.[33]
$\varphi_{DMC}$	0.1	-	Fit
$\varphi_{gas}$	0.2	-	Fit
$\rho$	2900	kg m <sup>-3</sup>	Calc

## 2.3 Fluid dynamics and combustion models

### 2.3.1 Fluid dynamics conservation equations

Once the vent valve is broken, the pressurized gas will jet and mix with the air and the mixture gases will be ignited when an ignition source exists around or the temperature reaches the ignition point of gases. Reynolds number at the top vent valve is employed to determine the flow regime in the air zone, as shown in Eqn.(31). According to the estimation of velocity from the previous step, the peak air flow velocity could reach 178.3 m s<sup>-1</sup>. Considering the typical range of values that the nozzle diameter is 10<sup>-2</sup> m, the dynamic gas viscosity is about 10<sup>-5</sup> Pa·s and the gas density is approximately 10<sup>0</sup> kg·m<sup>-3</sup>, the maximal Reynolds number for the venting gas flow can reach 178300 and the gas flow during TR is expected to be turbulent.

$$Re = \frac{\rho u d}{\mu} \sim 0 - 178300 \quad (31)$$

In this model, the flow in the air region is therefore computed by means of Reynolds-averaged Navier-

Stokes (RANS) equations. The conservation equations in the fluid region are shown as follows:

Mass conservation equation:

$$\frac{\partial \bar{\rho}}{\partial t} + \frac{\partial \bar{\rho} \bar{u}_j}{\partial x_j} = 0 \quad (32)$$

Momentum conservation equation:

$$\frac{\partial \bar{\rho} \bar{u}_j}{\partial t} + \frac{\partial \bar{\rho} \bar{u}_i \bar{u}_j}{\partial x_j} = \frac{\partial}{\partial x_j} \left( \rho(v + v_t) \left( \frac{\partial \bar{u}_i}{\partial x_j} + \frac{\partial \bar{u}_j}{\partial x_i} - \frac{2}{3} \frac{\partial \bar{u}_k}{\partial x_k} \delta_{ij} \right) \right) - \frac{\partial \bar{p}_d}{\partial x_i} - g_i x_i \frac{\partial \bar{p}}{\partial x_i} \quad (33)$$

Energy conservation equation:

$$\frac{\partial \bar{\rho} \bar{h}}{\partial t} + \frac{\partial \bar{\rho} \bar{u}_j \bar{h}}{\partial x_j} = \frac{D \bar{p}}{Dt} + \frac{\partial}{\partial x_j} \left[ \bar{\rho} \left( D + \frac{v_t}{Pr_t} \right) \frac{\partial \bar{h}}{\partial x_j} \right] + \dot{q}'' \quad (34)$$

Species transport equation:

$$\frac{\partial \bar{\rho} \bar{Y}_m}{\partial t} + \frac{\partial \bar{\rho} \bar{u}_j \bar{Y}_m}{\partial x_j} = \frac{\partial}{\partial x_j} \left[ \bar{\rho} \left( D + \frac{v_t}{Pr_t} \right) \frac{\partial \bar{Y}_m}{\partial x_j} \right] + \bar{\omega}_m \quad (35)$$

where  $\rho$ ,  $u$ ,  $p$ ,  $h$  and  $Y$  are the density, velocity, pressure, sensible enthalpy and mass fraction of gas mixture, respectively.  $v$ ,  $v_t$ ,  $D$  and  $Pr_t$  denote laminar dynamic viscosity, turbulent dynamic viscosity, laminar diffusion coefficient and turbulent Prantl number.  $\omega_m$  is production or sink rate of the gas species from the combustion reactions.  $\dot{q}''$  is the heat release rate per unit volume from the combustion reactions. The calculation of above thermos physical parameters can be found in the Table S2 and Table S3.

The traditional linear-eddy-viscosity RANS models is still the preference for the turbulence calculation in engineering application. In order to close the above equations, two transport equations for two turbulence properties are still needed. The  $k-\epsilon$  model is by far the most widely employed and tested two-equation model with many perfections incorporated over the years, and it behaves well in combustion prediction [67]. The details of the transport equations for turbulence kinetic energy  $k$  and turbulence dissipation rate  $\epsilon$  can be found in reference [68].

$$v_t = C_\mu \frac{k^2}{\varepsilon} \quad (36)$$

$$\frac{\partial k}{\partial t} + \bar{u}_j \frac{\partial k}{\partial x_j} = \frac{\partial}{\partial x_j} \left[ \frac{(v + v_t)}{\sigma_k} \frac{\partial k}{\partial x_j} \right] - c + \tau_y \frac{\partial \bar{u}_i}{\partial x_j} \quad (37)$$

$$\frac{\partial \varepsilon}{\partial t} + \bar{u}_j \frac{\partial \varepsilon}{\partial x_j} = \frac{\partial}{\partial x_j} \left[ \frac{(v + v_t)}{\sigma_\varepsilon} \frac{\partial \varepsilon}{\partial x_j} \right] + C_{\varepsilon 1} \frac{\varepsilon}{k} \tau_y \frac{\partial \bar{u}_i}{\partial x_j} - C_{\varepsilon 2} \frac{\varepsilon^2}{k} \quad (38)$$

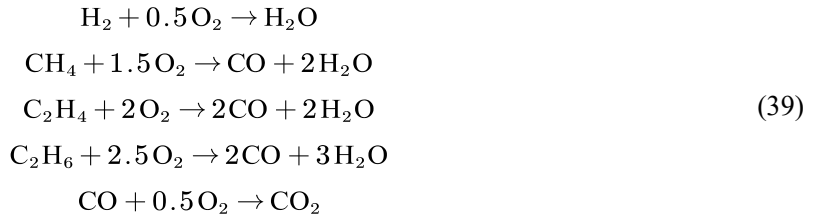
where  $\sigma_k = 1.0$  and  $\sigma_\varepsilon = 1.3$  are the Prandtl numbers for  $k$  and  $\varepsilon$  respectively.  $C_\mu = 0.09$ ,  $C_{\varepsilon 1} = 1.44$  and  $C_{\varepsilon 2} = 1.92$  are the model constants [67].

It should be mentioned that some solid particles will be ejected during TR, the main components of which is carbon accounting for approximately 68.0-69.0% [69]. Thus, the solid particles might be oxidized and produced some soot at high temperature of jet fire. The particles under oxidation and soot might be elevated temperature and radiated heat to the surroundings. However, the soot generation mechanism and dispersive states have not been clear yet, so the radiative heat loss from the solid particles and soot was neglected in the present simulation. This omission might incur 20 to 40% over prediction in the jet fire temperatures.

### 2.3.2 Reaction mechanism

The combustion of gas mixture is modelled through the eddy dissipation concept (EDC) [70]. The EDC model has been extensively used for simulations of turbulent reactive flows in the past resulting from its superiority of suiting finite rate chemistry with an affordable computational cost [71]. The gas released from the cell is considered to mainly consist of H<sub>2</sub>, CO, CO<sub>2</sub>, CH<sub>4</sub>, C<sub>2</sub>H<sub>4</sub> and C<sub>2</sub>H<sub>6</sub> from the previous experimental results[7-10]. It should be noted that some electrolyte vapor will be ejected along with the generation gases. However, the amount of venting electrolyte be negligible compared with the generation gases from thermal decomposition reactions, according to the previous experimental researches for the identification and quantification of release gases [7, 8, 10, 51]. In addition, Fernandes et al. [9] also reported that the gases released from the LIB cells had the same heat release rate as a DMC flame. Thus, the effect of electrolyte

vapor combustion on the heat release of jet fire is not considered. In this model, the reduced kinetics of hydrocarbon oxidation is modelled by two-step reaction mechanism while the burning of hydrogen is assumed as one-step reaction [40]:



The rates of chemical kinetics can be calculated from Arrhenius' law as shown in Eq.(40), and the parameters are summarized in **Table 4**.

$$\omega = A \exp(-Ea/RT) [\text{Fuel}]^a [\text{O}_2]^b [\text{H}_2\text{O}]^c \tag{40}$$

**Table 4**

Chemical kinetic parameters for gas combustion reactions (units in m, s, K, kJ, kmol).

Fuel	A	Ea	a	b	c
H <sub>2</sub>	1.04×10 <sup>9</sup>	1.00×10 <sup>3</sup>	1	0.5	0.0
CH <sub>4</sub>	2.80×10 <sup>9</sup>	2.43×10 <sup>3</sup>	-0.3	1.3	0.0
C <sub>2</sub> H <sub>4</sub>	1.35×10 <sup>10</sup>	1.51×10 <sup>3</sup>	0.1	1.65	0.0
C <sub>2</sub> H <sub>6</sub>	6.18×10 <sup>9</sup>	1.51×10 <sup>3</sup>	0.1	1.65	0.0
CO	2.24×10 <sup>12</sup>	2.01×10 <sup>3</sup>	1	0.25	0.5

### 2.3.3 Thermodynamic Properties

~~OpenFOAM contains numerous calculation models for thermal physical parameters based on temperature pressure system, and the calculation equations and methods are different pointing at various specific simulations. This section mainly introduces the determination and calculation method of main thermos physical parameters.~~

~~The enthalpy and heat capacity at constant pressure for the fluid components are temperature dependent and calculated based on the 7 coefficient NASA polynomials from JANAF thermochemical tables [72]:~~

$$C_p(T) = R(a_0 + a_1 T + a_2 T^2 + a_3 T^3 + a_4 T^4) \tag{41}$$

$$h(T) = R(a_0 T + a_1 T^2/2 + a_2 T^3/3 + a_3 T^4/4 + a_4 T^5/5 + b_1) \tag{42}$$

where  $a_1, a_2, \dots, a_7$ , and  $b_1$  are fitting coefficients. The dynamic viscosities  $\mu$  for the mixture components are also temperature dependent and calculated from Sutherland's law [73]:

$$\mu = \frac{A_s \sqrt{T}}{1 + T_s/T} \quad (43)$$

where  $A_s = 1.67212 \times 10^{-6} \text{ kg m}^3 \text{ s}^{-1} \text{ K}^{-1/2}$  and  $T_s = 170.672 \text{ K}$  are the two Sutherland coefficients. The thermal conductivity for the mixture components is expressed by the Eucken model [74]:

$$\kappa = \mu C_v \left( 1.32 + 1.77 \frac{R}{C_v} \right) \quad (44)$$

where  $C_v$  is the heat capacity at constant volume. The molecular thermal diffusivity  $D$  is calculated as:

$$D = \frac{\kappa}{C_{pv}} \quad (45)$$

where  $C_{pv}$  is the heat capacity at constant pressure/volume.

### 3. Experiments and model instantiation

#### 3.1 Experiments considered

To validate the developed novel TR model, some experiments have been carried out to measure the temperature data of the cell surface and the flame under thermal abuse. The battery used for the test was cylindrical 18650 LIB that has a capacity of 3.4 Ah, charge voltage of 4.2 V, nominal voltage of 3.6 V. The cathode material is  $\text{LiNi}_{0.8}\text{Co}_{0.15}\text{Al}_{0.05}\text{O}_2$  and the anode material is graphite. The electrolyte is composed of  $\text{LiPF}_6$  dissolved in organic solvents. Cells were pre-cycled using a cycler (Neware) at 0.1C current rate within 2.5–4.2 V for three cycles and then followed by a constant current charging to achieve 75% SOC.

As shown in Fig. 6, the cell was fixed in a specially designed metal fixture, exposed to the open air. The polyimide electrothermal film was used for heating, whose power and size are 32.5 W and 30 mm × 62.5 mm. Four 0.5 mm K-type chromel-alumel thermocouples with 0.5 s response time and ±1.0 °C accuracy were

employed to obtain the temperature data. One thermocouple marked as TC#1 is attached on the surface of the cell away from the heater to measure the temperature of the LIB cell surface. Three thermocouples marked as TC#2, TC#3 and TC#4 respectively were placed at 5 cm, 10 cm and 15 cm above the vent valve of the cell, aiming at measuring the flow temperature during the venting event and the flame temperature at different heights. Data measured during tests were recorded by the computer through the DAQ board. One high definition camera recording at 50 frames per second was placed about 0.5 m in front of the cell to capture the evolution of jet fire during TR. The cell was heated in the open air during the whole experimental process, which can be regarded as the natural convection heat transfer in infinite space. Once the TR occurred, the heater power was cut off immediately.

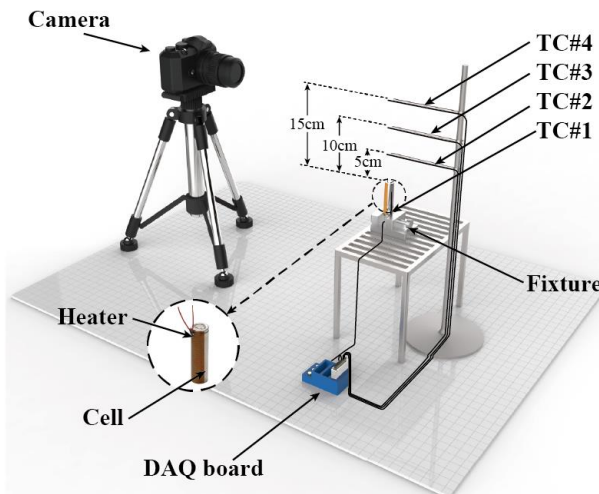


**Fig. 6.** Schematic of the experimental devices.

The Otsu's method [75] is used to process the experimental flame images to obtain the transient flame heights during TR. The original images are firstly converted to gray scale images with various luminance values. Based on its luminance value and a threshold value calculated from Otsu's method [75], a binary image can be obtained and then saved as a matrix in MATLAB® where each pixel was an element in the matrix. Then the flame height on each frame can be calculated based on the corresponding matrix and the

scale of the figure.

The significant errors in thermocouple readings may be caused by radiation and convection heat transfer between the thermocouple and the surrounding when used in the presence of flames. Thus, temperature corrections are essential for performing a temperature measurement of jet fire during TR with thermocouples.

The energy balance on the thermocouple probe can be expressed as:

$$(T - T_m) Nu \frac{\kappa}{d} = \sigma \varepsilon (T_m^4 - T_a^4) \quad (46)$$

where  $T$  is the gas temperature,  $T_m$  is the temperature at the thermocouple probe,  $T_a$  is the ambient temperature,  $\kappa$  is the gas thermal conductivity,  $d$  is the diameter of the thermocouple probe,  $\sigma$  is the Stefan–Boltzmann constant,  $\varepsilon$  is the thermocouple emissivity, and  $Nu$  is the Nusselt number given in Ref. [76]:

$$Nu = 2 + 0.6 Re^{1/2} Pr^{1/3} \quad (47)$$

where  $Re$  is the Reynolds number and  $Pr$  is the Prandtl number. The  $Re$  is estimated according the measured gas velocity in Ref. [77], and the temperature dependent gas properties for  $\kappa$ ,  $Re$  and  $Pr$  were taken as those of air and the temperature dependent emissivity was taken from Ref. [76]. A radiative correction for the gas temperature by solving above equations can be found less than 30 °C for the peak fire temperature of 1107 °C.

### 3.2 Simulation conditions

Following the above experimental conditions, a 2D numerical model has been built in OpenFOAM. The schematic of the computational geometry and mesh are illustrated in **Fig. 7**. The computational domain zone was divided into three zones, including air zone, heater zone and cell zone, with the size of 200 mm × 500 mm. The air zone was modeled as the fluid initially filled with 79.05% nitrogen and 20.95% oxygen. The cell zone was simplified as a homogeneous solid structure, aiming at reducing the computational cost to resolve all the small-scale thin layer structures. The heater zone was built by the solid zone with a constant

heat source to simulate the heating effect of the polyimide electrothermal film, and it was attached to both sides of cell zone, with a height of 62.5 mm and a thickness of 0.5 mm. The initial temperature of the whole region was set as 26.85 °C. The thermodynamic and gas generation parameters in **Table 1** and **Table 2**, estimated from Golubkov's experiments [51], are used to provide input data to address the influence of corresponding SOCs on the cell TR and venting behaviors.

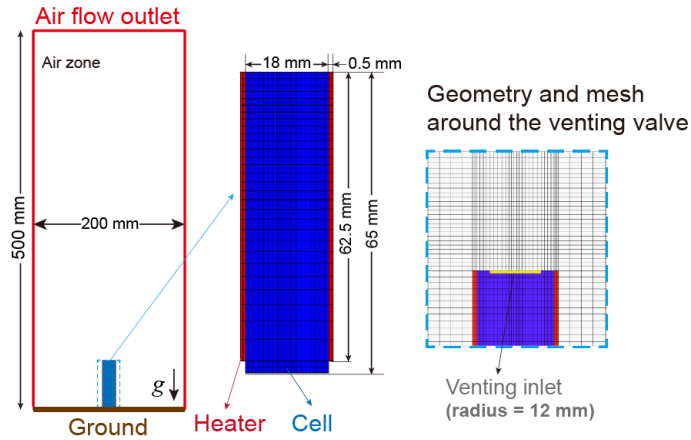


**Fig. 7.** Schematic of the computational model.

The boundary condition for the air zone consists of four parts: the ground, the solid wall between cell/heater and air, the venting inlet on the top of cell, the air flow outlet to ambience. For the velocity field, no-slip boundary conditions are prescribed at the venting inlet before the opening of safety valve, the solid wall and the ground. After the safety valve opened, the venting inlet was given a boundary condition of fixed value  $u_2$ . Considering the conduction, convection and radiation heat transfer, the temperature boundary condition between the cell/heater and air can be written as follows:

$$-\kappa_{\text{cell/heater}} \frac{\partial T}{\partial n} = -\kappa_{\text{air}} \frac{\partial T}{\partial n} + h_{\text{cell}} (T_{\text{air}} - T_{\text{cell/heater}}) + \varepsilon_{\text{cell}} \sigma (T_{\text{air}}^4 - T_{\text{cell/heater}}^4) \quad (48)$$

where  $\varepsilon_{\text{cell}}$  is the surface emissivity of the cell, and  $\sigma$  is Stefan-Boltzmann constant. where  $h_{\text{cell}}$  is convective heat transfer coefficient, calculated based on the empirical correlations between Nusselt number and Reynolds number [76]. The heat conduction dominates the contribution of heat transfer between solids, thus the boundary condition between the cell and heater is given as:

$$-\kappa_{\text{cell}} \frac{\partial T}{\partial n} = -\kappa_{\text{heater}} \frac{\partial T}{\partial n} \quad (49)$$

For the species field, zero gradient boundary conditions are prescribed at the exterior of cell before venting. Then a boundary condition of fixed mole fraction is applied at the venting inlet to simulate the open of safety valve and the outflow of gases. Owing to the complexity of gas generation mechanism and lack of the experimental data support for gas component fraction in real-time, the gas species and generation rate of each gas are hard to be determine at every temperature and time point during TR. Thus, the mole fraction of gas species flowing out the venting inlet is assumed to be constant during venting and combustion, but different with various SOCs, which is identified by Golubkov's experiments [51]. The mole fractions for each species at various SOCs are listed in **Table 5**. Then zero gradient boundary conditions will continue to be employed to simulate the end of TR process, when the venting velocity drops to zero. However, owing to the abrupt change of gas mole fraction, this assumption may cause the heat release rate dropped to zero immediately when the flame extinguished.

**Table 5**

The mole fractions for each species and various SOCs at the boundary condition of venting inlet (%)[51]

SOC (%)	H <sub>2</sub>	CO	CO <sub>2</sub>	CH <sub>4</sub>	C <sub>2</sub> H <sub>4</sub>	C <sub>2</sub> H <sub>6</sub>
25	15.5	5.5	62.5	8.7	7.5	-
50	17.5	39.9	33.8	5.2	3.2	0.4
75	24.2	43.7	20.8	7.5	3.3	0.5

Mesh sensitivity study was conducted for the cell at 75% SOC, using three meshes of different resolutions with 9612, 16000 and 24200 grid points. **Fig. 8** shows the temperature evolution of the cell with 75% SOC with different mesh resolutions. It can be seen that the mesh case with 9612 nodes shows different behavior in the peak temperature during TR and the grid number had trivial influence when it was greater than 16000 nodes, thus the mesh with 16000 nodes was employed in the subsequent simulations in the present study considering both accuracy and calculation efficiency.

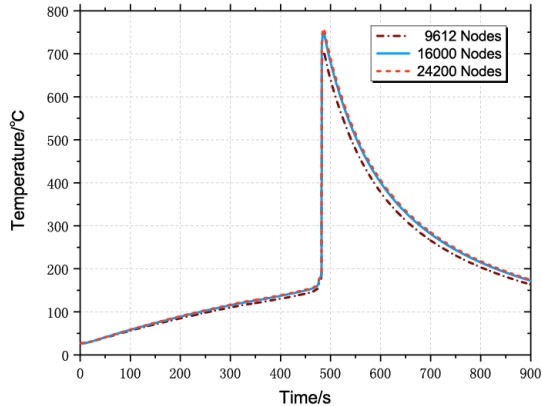


**Fig. 8.** Results of grid sensitivity study of the cell temperature at 75% SOC.

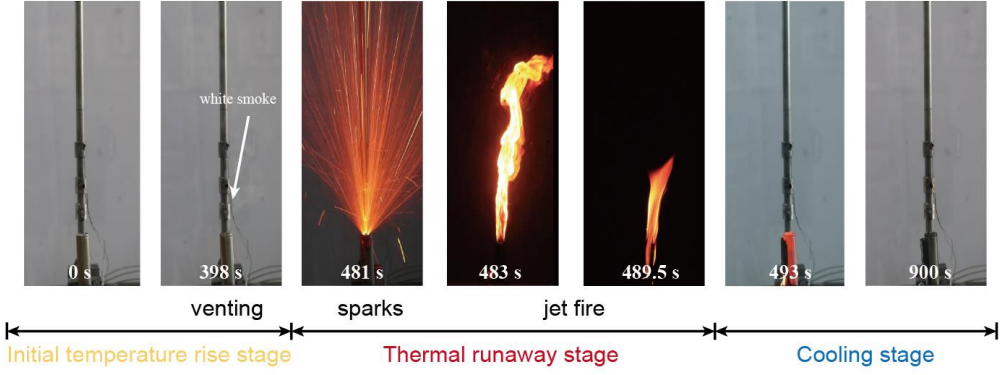
## 4. Results and discussion

### 4.1 Overall evolution under thermal abuse

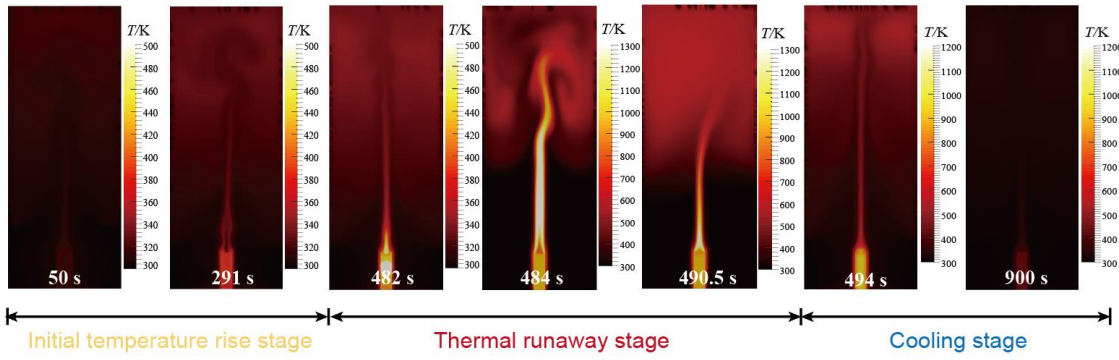
**Fig. 9** displays the comparison of the overall evolution for the cell under thermal abuse between experiments and simulation. The whole thermal abuse process of the cell can be divided into three stages with several key features: initial temperature rise, thermal runaway and cooling. Experimentally captured images are shown in **Fig. 9 (a)**. In the early stage of heating, no obvious phenomenon was observed visually, while the temperature starts rising from the data measured by thermocouple. The first phenomenon can be observed is a loud crack indicating the open of vent valve, and this is followed by an ejecting of white smoke and gases. Two typical phenomena during the TR stage are sparks and jet fire. Sparks with a reverse conical contour were ejected from vent valve of cell, and this process usually lasted 1.0~2.0 s. It is generally considered that the sparks consist of lithium salts, carbon, the aluminum from the melting current collector [69, 78], which present red-hot due to high temperature. After a brief extinction about 0.2~0.5 s, a torch-like jet fire was observed and then the flame height decreased gradually with the decrease of the cell internal pressure. The detailed evolution of the jet fire will be discussed in the following section. However, it should

be noted that the combustion of polyimide heater also contributed to the development of the jet fire, while the experiments could not separate the cell and heater immediately after TR. The extinction of flame marks the end of TR stage and the beginning of cooling stage. In the early cooling stages, the cell presented red-hot state due to the long wave radiation from the aluminum can with high temperature to surroundings. With the natural convection heat transfer between the cell surface and the surrounding air, the cell was cooled to the surrounding temperature and presented grayish white due to the oxidation of aluminum can surface.

The predicted temperature fields of the cell and air were shown in **Fig. 9 (b)** and revealed some phenomena that cannot be observed by the experiments. During the initial temperature rise stage, the predicted cell temperature starts to rise resulting from the heat flux of heater and heat generation from exothermic decomposition reactions. In addition, the temperature field in the air region was assumed to be due to natural convection. **The current model did not consider the ejection of sparks during the TR, which involves the transport of high temperature solid or liquid particles.** In addition, jet sparks were generally considered as ignition sources of the venting gases [78]. However, the rapid transition from the sparks and jet fire indicate that the venting gases might have self-ignited due to their temperatures being well above their auto ignition temperatures of the constituents. This is in line with the combustion model used which assumed that the combustion reactions occur when the venting gas temperature reaches the onset temperature of the reduced reactions. The simulation of jet fire is the focus of this study, and the details will be discussed in the following section. During the cooling stage, the simulation results reveal the process of the cell temperature decrease under thermal convection and radiation.



(a) Experiment results of the overall evolution for the cell under thermal abuse



(b) Simulation results of the overall evolution for the cell under thermal abuse

**Fig. 9.** Comparison of the overall evolution for the cell under thermal abuse between experiments (a) and simulation (b).

#### 4.2 Temperature evolution characteristics

The temperature prediction of the cell surface and flame for the cell with 75% SOC is compared with the experimental measurements as shown in **Fig. 10**. The temperature on the cell surface increases quite slowly when the cell is heated externally at a constant heating rate at the beginning, shown as the data of TC#1. In this stage, the temperature change is governed by the balance of heat flux into the cell from heater, heat generation from the decomposition reaction and the heat loss into air including thermal convection and radiation. With the cell temperature increase and the gas generation, the cell internal pressure increases and the venting event occurs at about 319 s when the cell temperature reaches 120 °C for simulation and 134 °C for experiment. The temperature data measured by TC#2 placed 5 cm above the cell captures the fluid temperature increase due to the ejecting of gases when the vent valve opens, and the venting gas flow

temperature is measured as 68.5 °C in experiments and simulated as 75.9 °C. With the development of thermal abuse, TR occurs at about 481 s when the cell temperature reaches TR onset temperature of 179.3 °C and then the temperature increases sharply to the TR peak temperature of 727.5 °C. Similar evolution can be observed in the simulation results that the TR onset temperature is about 183.6 °C and the TR peak temperature is approximately 748.8 °C. In the meanwhile, a jet fire was ejected from the top of cell due to the ignition of venting gases and the data from TC#2, TC#3 and TC#4 recorded the flame temperature at different heights. It can be seen from **Fig. 10** that the maximum measured flame temperatures were 1107 °C, 913 °C and 594 °C at 5 cm, 10 cm and 15 cm above the cell top, respectively while the predicted corresponding maximum temperatures were 1310 °C, 1091 °C and 856 °C for the same locations. **The maximum discrepancies between the predictions and measurements were hence within 30%. Fig. 10** indicates that the predicted peak temperature and onset time of TR are close to the measurements while the predicted flame temperature is slightly higher than the measured ones during TR. The marginal deviation is thought to be due to that the composition of the combustible gases being set according to previous studies for similar but different cells than the one considered here. Overall, the model is capable of simulating the complete processes of LIBs under thermal abuse from venting to fire evolution with reasonable accuracy in the predictions of the key thermal parameters, such as TR onset temperature, TR peak temperature and the flame temperature.

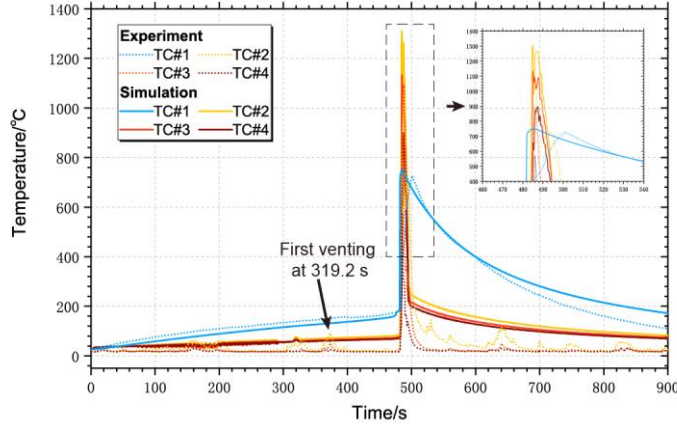


**Fig. 10.** Comparison of the measured and predicted temperature of the cell surface and flame for NCA cell with 75% SOC.

**Fig. 11** compares the temperature curves of the cell surface and the flame at different heights for cells with 25% SOC and 50% SOC. The air temperature increase caused by the first venting event can be observed from **Fig. 11** that the air temperature above the venting valve 5 cm reaches about 95.9 °C and 95.7 °C for the cell with 25% SOC and 50% SOC while that shows a lower value of 75.9 °C for 75% SOC as plotted in **Fig. 10**. The lower venting temperature  $T_2$  may be responsible for the above divergence that the cell with 75% SOC first vents at a lower cell temperature than other cells. **Fig. 10** and **Fig. 11** show that the TR onset temperatures are 226 °C, 215 °C and 190 °C for the cell with 25% SOC, 50% SOC and 75% SOC, respectively. Correspondingly, the onset time of TR increases with the increasing TR onset temperature, which is 940 s, 906 s, 617 s and 481 s for the cell with 25% SOC, 50% SOC and 75% SOC. The results indicate that the SOC of cells has a significant influence on the thermal safety that the cells with a high SOC generally face a higher TR risk. It can be seen from **Fig. 11** (a) that the maximum air temperatures during TR are 461 °C at 5 cm, 379 °C at 10 cm and 335 °C at 15 cm respectively for the cell with 25% SOC. The simulation results show that the air temperature increase results from the heat load of extremely elevated temperature ejecting instead of the combustion of mixture gases. In contrast to the cell with 25% SOC, the **Fig. 11** (b) shows a more intense temperature rise above the cell caused by the fire for the cell with 50% SOC, which are 989 °C

at 5 cm, 744 °C at 10 cm and 606 °C at 15 cm separately. As mentioned before, the higher maximum flame temperature at different heights can be captured for the cell with 75% SOC. Totally, the increase of cell SOC shortens the onset time of venting and TR event, as well as results in a higher flame temperature. Hence, the cells with higher SOC in LIB modules are inclined to cause TR propagation owing to a larger thermal loads from fire but a smaller thermal tolerance.

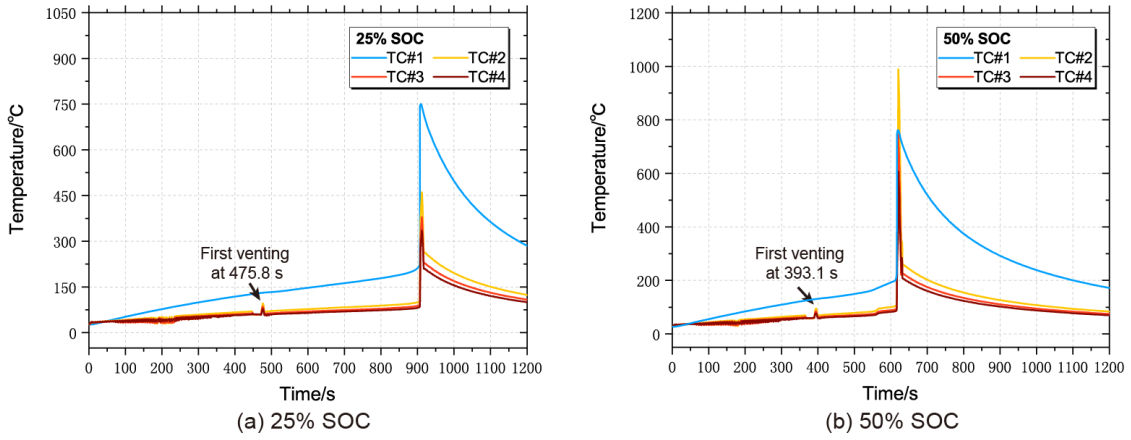


**Fig. 11.** The temperature variations of the cell surface and the flame at different heights for cells with 25% SOC (a) and 50% SOC (b).

#### 4.3 Internal pressure and venting characteristics

The plots in **Fig. 12** illustrate the dynamic evolution of the cell internal pressure as well as the average temperature for the cell with various SOCs. The simulation plots capture the two pressure peaks: one peak at the time of vent valve opening and another caused by TR. It can be found from **Fig. 12** that the first venting event occurs at about 475 s when the temperature reaches about 131 °C for the cell with 25% SOC. With the increase of SOC, the onset time of the first venting event advances and that is 393 s for the cell with 50% SOC and 319 s for 75% SOC, and their average temperatures are about 124 °C and 112 °C. The onset time of the first venting event is determined by the time when the cell internal pressure reaches the critical pressure while the internal pressure is governed by the partial pressure of the electrolyte vapor and generated gases.

For the cells with high SOC, the higher rate of thermal abuse reaction leads to a faster temperature rise and gas generation, and the rapid pressure accumulation ultimately results in the earlier venting event. Then the cell internal pressure reduces sharply to the ambient pressure after the initial venting, and the second time venting event occurs when the cell goes into TR. **The occurrence of the 2<sup>nd</sup> venting event results from the sharp rise of temperature and the massive generation of gas from thermal decomposition reactions during TR.**

It is noteworthy that the peak pressures of the second time venting present a positive correlation with SOCs, which are approximately  $1.63 \times 10^5$  Pa for 25% SOC,  $3.01 \times 10^5$  Pa for 50% SOC and  $4.03 \times 10^5$  Pa for 75% SOC. The magnitude of pressure increase inside the cell during the second time venting is determined by three aspects: the temperature rise rate  $dT/dt$ , the gas generation rate and the flow characteristics through venting valve. The temperature rise rate is affected by the abuse reaction rate and enthalpy, and the gas generation rate is determined by the abuse reaction rate and corresponding gas quantity. The mechanism of flow characteristics is complex, one influence factor is the structure of vent cap, such as the vent opening area, and another is the effect of ambient conditions on jetting, such as ambient pressure and obstruction. Thus, the higher rate of thermal abuse reaction and larger gas generation quantity are responsible for the significant pressure rise for the cells with higher SOC during TR.

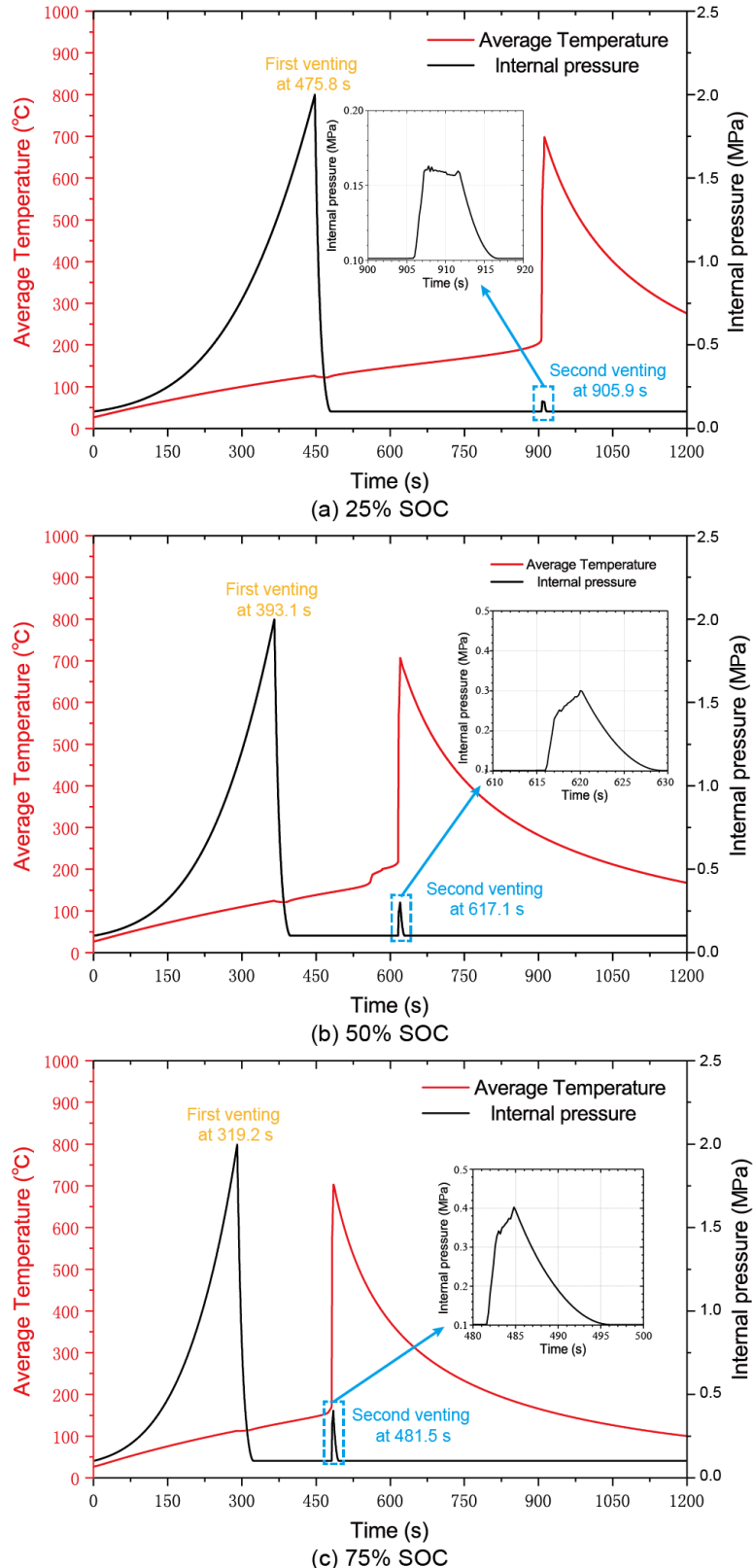


**Fig. 12.** The variations of average temperature and internal pressure for the cell with 25% SOC (a), 50% SOC (b) and 75% SOC (c) under thermal abuse.

**Fig. 13** shows the gas flow velocity and Mach number variations at Level 2 for the cell with 25% SOC,

50% SOC and 75% SOC. Corresponding to the evolution of the cell internal pressure, two violent ejection events can be found. The first-time venting event occurs when the safety valve opens, and the flow velocity  $u_2$  all reaches the local sonic velocity of  $111.8 \text{ m s}^{-1}$  for the cell with various SOCs. It can be noted the flow velocity  $u_2$  is the same for various SOCs, which results from the identical critical pressure of the open of venting valve for the first-time venting. When the LIBs go into TR, another ejection event occurs owing to the severe temperature rise and gas generation. The gas flow for the cell with 25% SOC is subsonic with the peak  $Ma$  of 0.848 as shown in **Fig. 13** (a), and the peak speed of gas flow at Level 2 is about  $148.1 \text{ m s}^{-1}$ . The peak  $Ma$  of gas flows for the cells with 50% SOC and 75% SOC all reach 1.0, indicating their flows are choked flow, and their peak flow velocity is  $178.3 \text{ m s}^{-1}$ . However, compared with the cell with 50% SOC, the duration of choked flow is found to be longer for the cell with 75% SOC, which indicates the amount of the gases ejected during TR is larger at this situation. In addition, the lasting time of the second time venting events is found to be the same for the cells with various SOCs, and the whole venting procedure lasted about 11 s. It should be noticed that the flow velocity during TR is higher than that at the first venting event although the cell internal pressure is much larger at the first venting event. The flow velocity is related to the local sonic velocity and the local sonic velocity is positively correlated with the temperature, thus the rising ejected gas temperature during TR results in the higher local sonic velocity. In this case, the flow velocity during TR is higher at the same Mach number.

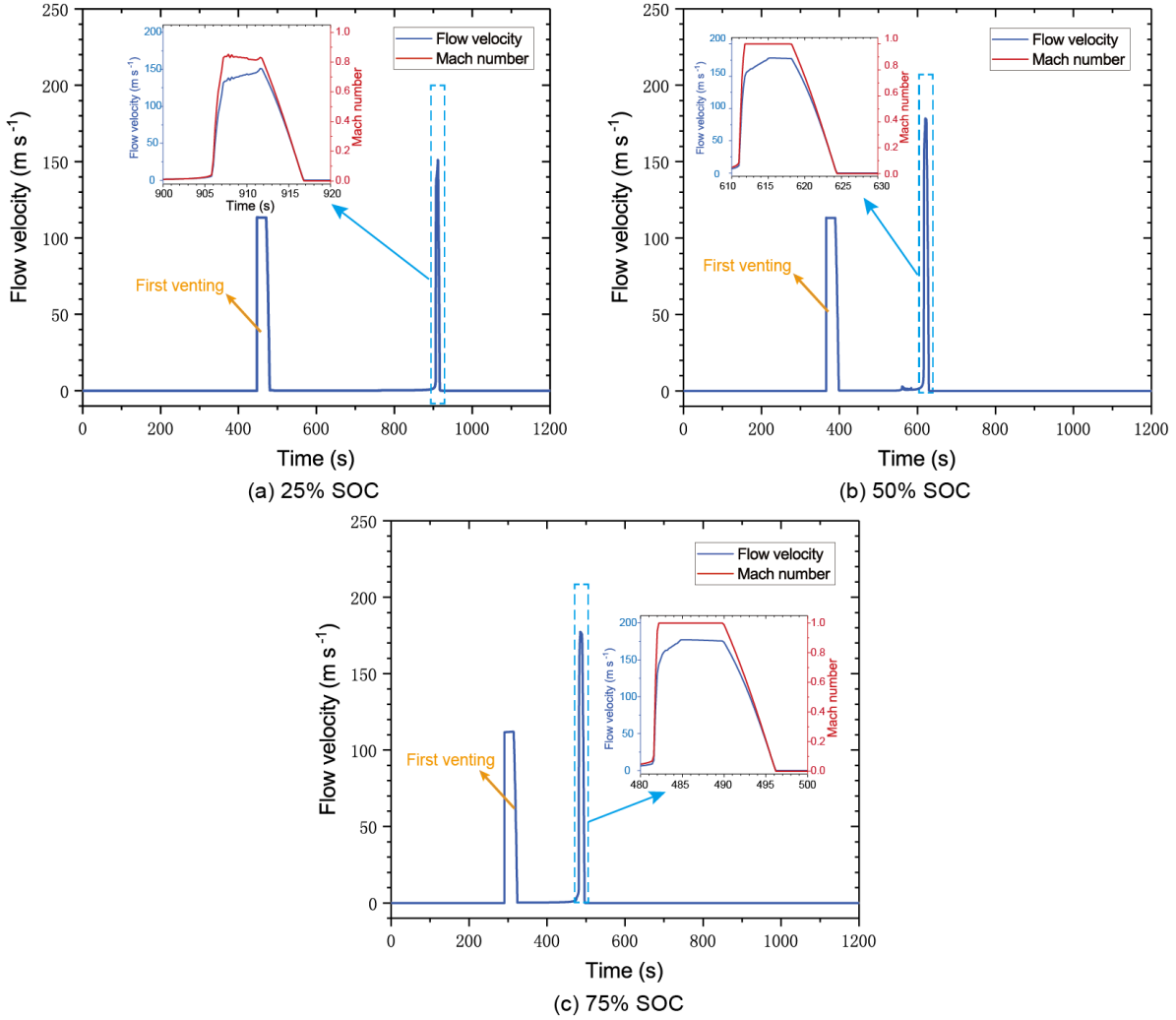


**Fig. 13.** The variations of the flow velocity and Mach number at Level 2 for the cell with 25% SOC (a), 50% SOC (b) and 75% SOC (c).

#### 4.4 Jet fire characteristics

The temporal evolution comparison of the jet fire between the experiments and simulation for the cell with 75% SOC as well as the comparison between various SOCs are illustrated in **Fig. 14**. The jet fire evolution images captured by the camera is presented in **Fig. 14 (a)**. In the early stage of combustion, the flame spread rapidly upwards and the flame height reached the peak within 1 s. Then the effect of buoyancy gradually governed the turbulent diffusion of jet fire with the attenuation of momentum and the flame height was observed to decrease gradually and eventually extinct after burning for approximately 11 s. The flame

color could be found to change from white to yellow and brightness gradually weakened. In addition, the decrease of flame width with time could be also observed. The temperature field with a legend range from 23 °C to 1023 °C is employed as the predicting jet fire evolution for the cell with 75% SOC, to be compared with the experiments, as shown in **Fig. 14** (b). It should be noted that the flame color and brightness in measured images were not exactly corresponding to temperature range in simulation images, hence the predicted and measure flame shapes presented in **Fig. 14** (a) and (b) are not necessarily fully consistent. However, the similarities of flame evolution between them are apparent.

**Fig. 14** (c) and (d) plot the time evolution of the temperature field during TR for the cell with 50% SOC and 25% SOC. Compared with the fire behaviors of cells at 75% SOC, the combustion behaviors are observed but the flame height and the radial flame width are significantly less than that at 75% SOC. The reason may lie in that the lower concentration of combustible gases and ejecting velocity lead to a light combustion. **Fig. 14** (d) shows that the cell with 25% SOC does not present as violent a temperature rise from exothermic combustion reactions, which may result from that the lower fraction of combustible gases is not sufficient to support a sustained combustion. However, it should be noted that the extremely elevated temperature ejecting gases during TR may still apply a heat load to the air and the upper cell in axial direction.

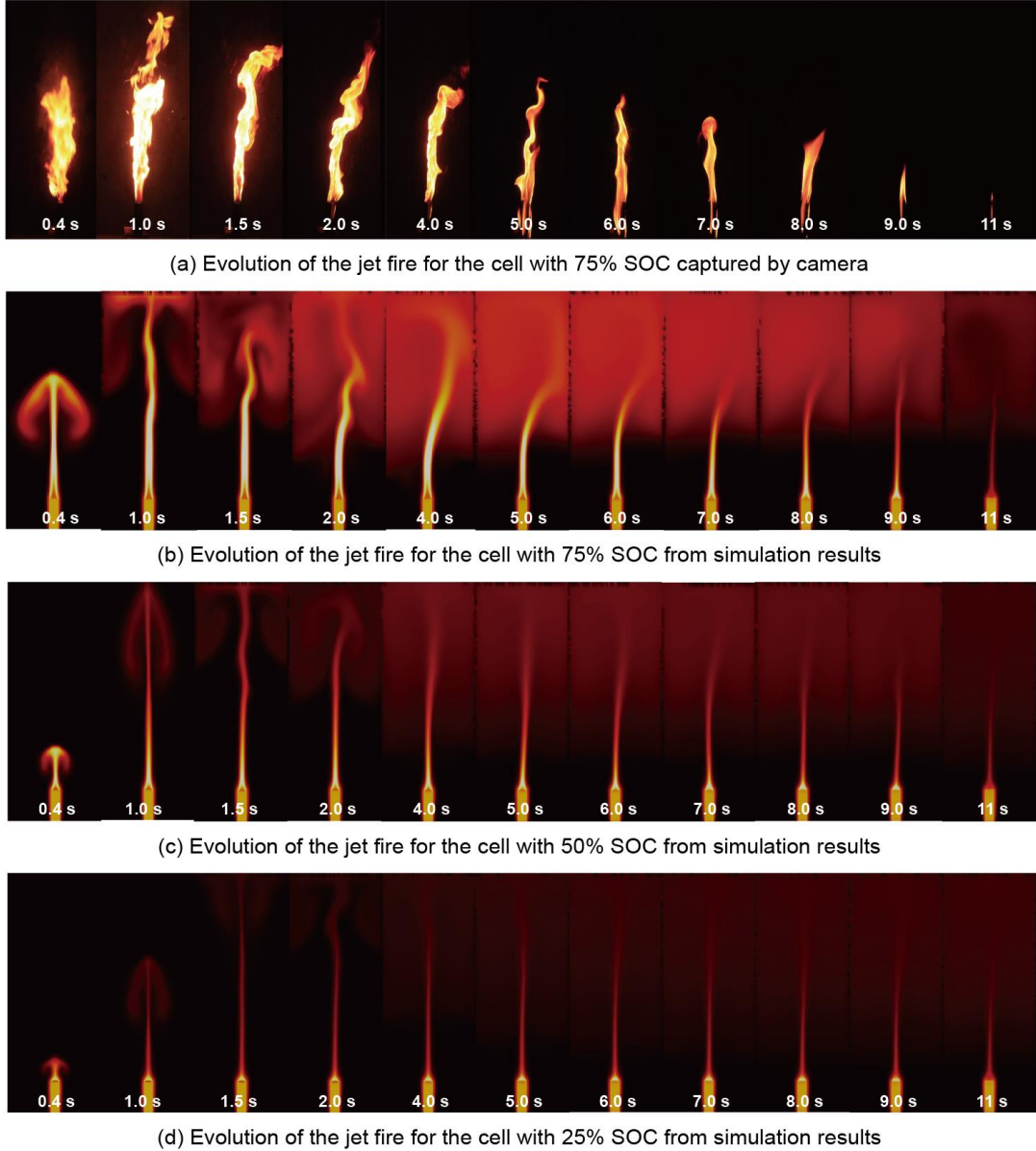


**Fig. 14.** Temporal evolution of jet fire images from experiments at 75% SOC (a) and the temperature field evolution during thermal runaway from simulation for the cells with 75% SOC (b), 50% SOC (c) and 25% SOC (d).

The predicted flame heights are also compared with the experimental measurements. The measured flame heights were obtained by MATLAB® as previously mentioned while the predicted flame height was calculated at the end of each time step from:

$$L_f = \max(\hat{x} \cdot \hat{g})|_{\tilde{Y}_{ref} \geq 0} \quad (50)$$

where  $\hat{x}$  is a vector representing the coordinate location of cell center, and  $\hat{g}$  is a unit vector indicating the reverse direction of gravitational acceleration.  $\tilde{Y}_{ref}$  is the stoichiometric condition of the reference species

including fuel and oxygen.

**Fig. 15** (a) plots the transient flame heights measured by three repeated experiments. The onset of ignition after TR is taken as the start time ( $t = 0$ ) in **Fig. 15** (a) and the flame height is recorded until the flame is invisible. It can be found that the flame height rapidly increased to the peak once the fire was ignited and then a general reduction trend in flame height could be observed until the flame was extinguished. The maximum flame heights were 337.3 mm, 353.5 mm and 290.5 mm and the estimated flame lasted about 7.37 s, 7.89 s and 8.58 s, respectively for the three tests. The average flame height of three repeated experiments is compared with the numerical simulation results to validate the accuracy of combustion prediction, as shown in **Fig. 15** (b). Reasonably good agreement has been achieved between the predicted and measured flame heights. In particular, the maximum flame height and the flame duration are consistent. However, a more obvious flame fluctuation can be observed in the experimental results in comparison with the predictions. This discrepancy might have been caused by a combination of variations in ejection velocity, gas composition and ejected solid particles during experiments.

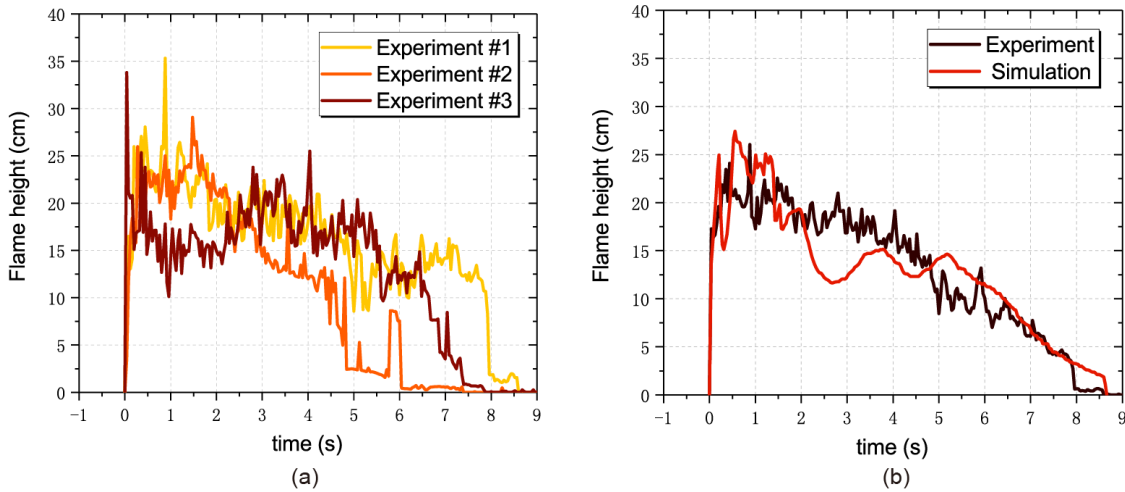


**Fig. 15.** The flame heights measured by repeated experiments (a) and the comparison between average flame height from experiments and simulation results (b).

**Fig. 16** (a) shows the transient variations of flame heights for the cells with various SOCs. It can be seen

that the flame heights increase with the rise of LIB SOCs, and that are 18.3 mm, 123.5 mm and 273.6 mm, respectively for the cell with 25% SOC, 50% SOC and 75% SOC. **Fig. 16 (b)** shows the transient variations of heat release rate for the cells with various SOCs. It can be found the peak HHRs for 25% SOC, 50% SOC and 75% SOC are 0.16 kW, 0.49 kW and 1.24 kW respectively. The calculated HHRs are larger than the previously reported peak HRRs of  $0.154 \pm 0.026$  kW for the 18650 LIBs with NCM cathode and 50% SOC [19], but lower than the HRRs measured by Chen et al. [78] for the 21700 LIBs with NCM cathode and 100% SOC, with the value of  $2.88 \pm 0.68$  kW. The marginal deviation is thought to be owing to the difference of LIB materials and specifications, but their order of magnitude for HRRs is similar. It can be noted that there is still a little heat release in spite of no obvious combustion phenomenon for the cell with 25% SOC, which indicates that a lower concentration of reactive gases still reacts near the venting valve. The total heat release from the combustion can be calculated from the integral of curve in **Fig. 16 (b)**, which are 1.17 kJ for 25% SOC, 3.21 kJ for 50% SOC and 8.05 kJ for 75% SOC. The total amount and concentration of combustible gases are responsible for the diversity of the total heat release from combustion at various SOCs. Some nonflammable gases, such as carbon dioxide, account for the majority of venting gases at lower SOC, while the reactive gases such as hydrogen, carbon monoxide and methane, contribute to the majority at higher SOC. Hence the increase of LIB SOC results in a larger amount of combustion heat generation, but also indicates a higher hazard of fire. In summary, the simulation results indicate that SOC has a significant effect on the jet fire characteristics of LIBs and the peak flame heights and HRRs present a remarkable growth trend with the increase of LIB SOCs.

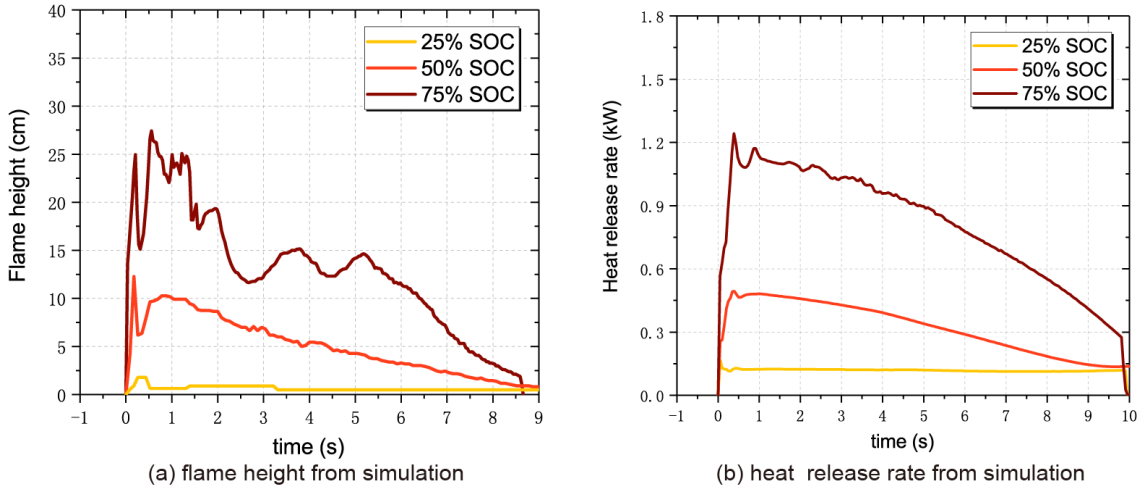


**Fig. 16.** The variations of flame heights (a) and heat release rate (b) for the cell with 25% SOC, 50% SOC and 75% SOC.

## 5. Conclusions

A coupled numerical model based on conjugate heat transfer has been developed with the frame of OpenFOAM. The lumped model was employed to predict the thermal abuse reactions and jet dynamics, while the gas flow and combustion reactions outside cell were solved numerically. The developed model captured well the onset time of thermal runaway at 481 s, consistent with the experiment. The predicted cell surface and air temperatures at three selected locations have achieved reasonably good agreement with the measurements that maximum discrepancies were within 30%. The validated model has subsequently been used to examine the effect of SOC on TR evolution and the subsequent jet. The following specific conclusions can also be drawn:

- (1) The ejecting of gases results in an abrupt temperature rise of the air above the cell when the venting valve opens. Increasing SOCs of the cells can shorten the onset time of thermal runaway and lead to increased maximum flame temperature at different heights.
- (2) The predicted cell internal pressure has highlighted the existence of two peaks with the 1<sup>st</sup> peak at the time of vent valve opening and 2<sup>nd</sup> peak at the onset of TR. The peak cell internal pressures and speeds

of gas flow in the second time venting are  $1.63 \times 10^5$  Pa and  $148.1 \text{ m s}^{-1}$  for 25% SOC,  $3.01 \times 10^5$  Pa and  $178.3 \text{ m s}^{-1}$  for 50% SOC,  $4.03 \times 10^5$  Pa and  $178.3 \text{ m s}^{-1}$  for 75% SOC, which indicates higher SOCs cause a more violent ejection during thermal runaway.

(3) The simulation presents the temporal evolution of jet fire while no obvious flame can be observed for cells at 25% SOC owing to a lower fraction of combustible gases. The peak flame heights are 18.3 mm, 123.5 mm and 273.6 mm and peak heat release rates are 0.16 kW, 0.49 kW and 1.24 kW for 25% SOC, 50% SOC and 75% SOC respectively, which present a growth trend with the increase of SOCs.

The newly developed model extends our previous efforts to model thermal runaway by combining the thermal decomposition reactions, pressure build-up and venting mechanisms and combustion process. The model represents the first step towards predicting TR propagation considering effects of jet fire and different modes of heat transfer in groups of LIB cells or modules. In future work, the influence of spark ejection and radiant heat feedback on jet fire will be incorporated and the simulation will also be extended into the explosion behavior for cell at higher SOC.

## Acknowledgements

This work is financially supported by the National Natural Science Foundation of China (Grant No.52174225 and Grant No.51604297). This work is also supported by the Individual Fellowship Scheme of the European Union's Horizon 2020 Marie Skłodowska-Curie Actions (Grant No. 896195, LiBTR), which funded Dr. Kong's fellowship at the University of Warwick.

## References

- [1] Qin P, Sun J, Yang X, Wang Q. Battery thermal management system based on the forced-air convection: A review. *eTransportation*. 2021;7:100097.

- [2] Liu T, Yang X-G, Ge S, Leng Y, Wang C-Y. Ultrafast charging of energy-dense lithium-ion batteries for urban air mobility. *eTransportation*. 2021;7:100103.
- [3] Ren D, Hsu H, Li R, Feng X, Guo D, Han X, et al. A comparative investigation of aging effects on thermal runaway behavior of lithium-ion batteries. *eTransportation*. 2019;2:100034.
- [4] Darcovich K, Laurent T, Ribberink H. Improved prospects for V2X with longer range 2nd generation electric vehicles. *eTransportation*. 2020;6:100085.
- [5] Zhang Y, Wang H, Li W, Li C. Quantitative identification of emissions from abused prismatic Ni-rich lithium-ion batteries. *eTransportation*. 2019;2:100031.
- [6] Cai T, Valecha P, Tran V, Engle B, Stefanopoulou A, Siegel J. Detection of Li-ion battery failure and venting with Carbon Dioxide sensors. *eTransportation*. 2021;7:100100.
- [7] Yuan L, Dubaniewicz T, Zlochower I, Thomas R, Rayyan N. Experimental study on thermal runaway and vented gases of lithium-ion cells. *Process Safety and Environmental Protection*. 2020.
- [8] Chen S, Wang Z, Wang J, Tong X, Yan W. Lower explosion limit of the vented gases from Li-ion batteries thermal runaway in high temperature condition. *Journal of Loss Prevention in the Process Industries*. 2020;63:103992.
- [9] Fernandes Y, Bry A, de Persis S. Identification and quantification of gases emitted during abuse tests by overcharge of a commercial Li-ion battery. *Journal of Power Sources*. 2018;389:106-19.
- [10] Golubkov AW, Fuchs D, Wagner J, Wiltsche H, Stangl C, Fauler G, et al. Thermal-runaway experiments on consumer Li-ion batteries with metal-oxide and olivin-type cathodes. *RSC Advances*. 2014;4:3633-42.
- [11] Feng X, He X, Ouyang M, Lu L, Wu P, Kulp C, et al. Thermal runaway propagation model for designing a safer battery pack with 25Ah LiNixCoyMnzO2 large format lithium ion battery. *Applied Energy*. 2015;154:74-91.
- [12] Feng X, Lu L, Ouyang M, Li J, He X. A 3D thermal runaway propagation model for a large format lithium ion battery module. *Energy*. 2016;115:194-208.
- [13] Li Q, Yang C, Santhanagopalan S, Smith K, Lamb J, Steele LA, et al. Numerical investigation of thermal runaway mitigation through a passive thermal management system. *Journal of Power Sources*. 2019;429:80-8.
- [14] Yuan C, Wang Q, Wang Y, Zhao Y. Inhibition effect of different interstitial materials on thermal runaway propagation in the cylindrical lithium-ion battery module. *Applied Thermal Engineering*. 2019;153:39-50.
- [15] Coman PT, Darcy EC, Veje CT, White RE. Numerical analysis of heat propagation in a battery pack using a novel technology for triggering thermal runaway. *Applied Energy*. 2017;203:189-200.
- [16] Xu J, Lan C, Qiao Y, Ma Y. Prevent thermal runaway of lithium-ion batteries with minichannel cooling. *Applied Thermal Engineering*. 2017;110:883-90.
- [17] Mohammed AH, Esmaeeli R, Aliniagerdroudbari H, Alhadri M, Hashemi SR, Nadkarni G, et al. Dual-purpose cooling plate for thermal management of prismatic lithium-ion batteries during normal operation and thermal runaway. *Applied Thermal Engineering*. 2019;160:114106.
- [18] Jindal P, Kumar BS, Bhattacharya J. Coupled electrochemical-abuse-heat-transfer model to predict thermal runaway propagation and mitigation strategy for an EV battery module. *Journal of Energy Storage*. 2021;39:102619.
- [19] Liu X, Wu Z, Stoliarov SI, Denlinger M, Masias A, Snyder K. Heat release during thermally-induced failure of a lithium ion battery: Impact of cathode composition. *Fire Safety Journal*. 2016;85:10-22.
- [20] Liu X, Stoliarov SI, Denlinger M, Masias A, Snyder K. Comprehensive calorimetry of the thermally-induced failure of a lithium ion battery. *Journal of Power Sources*. 2015;280:516-25.
- [21] Said AO, Lee C, Liu X, Wu Z, Stoliarov SI. Simultaneous measurement of multiple thermal hazards associated with a failure of prismatic lithium ion battery. *Proceedings of the Combustion Institute*. 2019;37:4173-

80.

- [22] Liu P, Li Y, Mao B, Chen M, Huang Z, Wang Q. Experimental study on thermal runaway and fire behaviors of large format lithium iron phosphate battery. *Applied Thermal Engineering*. 2021;192:116949.
- [23] Fu Y, Lu S, Li K, Liu C, Cheng X, Zhang H. An experimental study on burning behaviors of 18650 lithium ion batteries using a cone calorimeter. *Journal of Power Sources*. 2015;273:216-22.
- [24] Ping P, Wang Q, Huang P, Li K, Sun J, Kong D, et al. Study of the fire behavior of high-energy lithium-ion batteries with full-scale burning test. *Journal of Power Sources*. 2015;285:80-9.
- [25] Wang Q, Huang P, Ping P, Du Y, Li K, Sun J. Combustion behavior of lithium iron phosphate battery induced by external heat radiation. *Journal of Loss Prevention in the Process Industries*. 2017;49:961-9.
- [26] Ping P, Kong D, Zhang J, Wen R, Wen J. Characterization of behaviour and hazards of fire and deflagration for high-energy Li-ion cells by over-heating. *Journal of Power Sources*. 2018;398:55-66.
- [27] Wang Z, Yang H, Li Y, Wang G, Wang J. Thermal runaway and fire behaviors of large-scale lithium ion batteries with different heating methods. *Journal of Hazardous Materials*. 2019;379:120730.
- [28] Johnsplass J, Henriksen M, Vaagsaether K, Lundberg J, Bjerketvedt D. Simulation of burning velocities in gases vented from thermal run-a-way lithium ion batteries2017.
- [29] Larsson F, Anderson J, Andersson P, Mellander B-E. Thermal Modelling of Cell-to-Cell Fire Propagation and Cascading Thermal Runaway Failure Effects for Lithium-Ion Battery Cells and Modules Using Fire Walls. *Journal of The Electrochemical Society*. 2016;163:A2854-A65.
- [30] Hatchard TD, MacNeil DD, Basu A, JR D. Thermal model of cylindrical and prismatic lithium-ion cells. *Electrochem Soc*. 2001;148(7):A755.
- [31] Kim G-H, Pesaran A, Spotnitz R. A three-dimensional thermal abuse model for lithium-ion cells. *Journal of Power Sources*. 2007;170:476-89.
- [32] Ping P, Wang Q, Chung Y, Wen J. Modelling electro-thermal response of lithium-ion batteries from normal to abuse conditions. *Applied Energy*. 2017;205:1327-44.
- [33] Paul T. Coman, Eric C. Darcy, Christian T. Veje, White RE. Modelling Li-Ion Cell Thermal Runaway Triggered by an Internal Short Circuit Device Using an Efficiency Factor and Arrhenius Formulations. *Journal of the Electrochemical Society*. 2017;164: A587-A593.
- [34] Liang G, Zhang Y, Han Q, Liu Z, Jiang Z, Tian S. A novel 3D-layered electrochemical-thermal coupled model strategy for the nail-penetration process simulation. *Journal of Power Sources*. 2017;342:836-45.
- [35] Coman PT, Rayman S, White RE. A lumped model of venting during thermal runaway in a cylindrical Lithium Cobalt Oxide lithium-ion cell. *Journal of Power Sources*. 2016;307:56-62.
- [36] Coman PT, Mátéfi-Tempfli S, Veje CT, White RE. Modeling Vaporization, Gas Generation and Venting in Li-Ion Battery Cells with a Dimethyl Carbonate Electrolyte. *Journal of The Electrochemical Society*. 2017;164:A1858-A65.
- [37] Ostanek JK, Li W, Mukherjee PP, Crompton KR, Hacker C. Simulating onset and evolution of thermal runaway in Li-ion cells using a coupled thermal and venting model. *Applied Energy*. 2020;268:114972.
- [38] Mao B, Zhao C, Chen H, Wang Q, Sun J. Experimental and modeling analysis of jet flow and fire dynamics of 18650-type lithium-ion battery. *Applied Energy*. 2021;281:116054.
- [39] Bugryniec PJ, Davidson DJN, Brown DSF. Advanced abuse modelling of Li-ion cells – A novel description of cell pressurisation and simmering reactions. *Journal of Power Sources*. 2020;474:228396.
- [40] Kim J, Mallarapu A, Finegan DP, Santhanagopalan S. Modeling cell venting and gas-phase reactions in 18650 lithium ion batteries during thermal runaway. *Journal of Power Sources*. 2021;489:229496.
- [41] Defraeye T, Blocken B, Derome D, Nicolai B, Carmeliet J. Convective heat and mass transfer modelling at air–porous material interfaces: Overview of existing methods and relevance. *Chemical Engineering Science*.

2012;74:49-58.

- [42] Wang Q, Mao B, Stolarov SI, Sun J. A review of lithium ion battery failure mechanisms and fire prevention strategies. *Progress in Energy and Combustion Science*. 2019;73:95-131.
- [43] Wang Q, Ping P, Zhao X, Chu G, Sun J, Chen C. Thermal runaway caused fire and explosion of lithium ion battery. *Journal of Power Sources*. 2012;208:210-24.
- [44] Wang Q, Sun J, Yao X, Chen C. Thermal Behavior of Lithiated Graphite with Electrolyte in Lithium-Ion Batteries. *Journal of The Electrochemical Society*. 2006;153:A329-A33.
- [45] Spotnitz R, Franklin J. Abuse behavior of high-power, lithium-ion cells. *Journal of Power Sources*. 2003;113:81-100.
- [46] Mao B, Chen H, Cui Z, Wu T, Wang Q. Failure mechanism of the lithium ion battery during nail penetration. *International Journal of Heat and Mass Transfer*. 2018;122:1103-15.
- [47] Wang Y, Jiang J, Dahn JR. The reactivity of delithiated  $\text{Li}(\text{Ni1/3Co1/3Mn1/3})\text{O}_2$ ,  $\text{Li}(\text{Ni0.8Co0.15Al0.05})\text{O}_2$  or  $\text{LiCoO}_2$  with non-aqueous electrolyte. *Electrochemistry Communications*. 2007;9:2534-40.
- [48] Wang Q, Sun J, Yao X, Chen C. Micro calorimeter study on the thermal stability of lithium-ion battery electrolytes. *Journal of Loss Prevention in the Process Industries*. 2006;19:561-9.
- [49] Balakrishnan PG, Ramesh R, Prem Kumar T. Safety mechanisms in lithium-ion batteries. *Journal of Power Sources*. 2006;155:401-14.
- [50] Kong D, Wang G, Ping P, Wen J. Numerical investigation of thermal runaway behavior of lithium-ion batteries with different battery materials and heating conditions. *Applied Thermal Engineering*. 2021;189:116661.
- [51] Golubkov AW, Scheikl S, Planteu R, Voitic G, Wiltsche H, Stangl C, et al. Thermal runaway of commercial 18650 Li-ion batteries with LFP and NCA cathodes – impact of state of charge and overcharge. *RSC Advances*. 2015;5:57171-86.
- [52] Fang Y-J, Qian J-M. Isobaric Vapor–Liquid Equilibria of Binary Mixtures Containing the Carbonate Group  $-\text{OCOO}-$ . *Journal of Chemical & Engineering Data*. 2005;50:340-3.
- [53] Pasquier AD, Disma F, Bowmer T, Gozdz AS, Amatucci G, Tarascon JM. Differential Scanning Calorimetry Study of the Reactivity of Carbon Anodes in Plastic Li - Ion Batteries. *Journal of The Electrochemical Society*. 1998;145:472-7.
- [54] Aurbach D, Zaban A, Gofer Y, Ely YE, Weissman I, Chusid O, et al. Recent studies of the lithium-liquid electrolyte interface Electrochemical, morphological and spectral studies of a few important systems. *Journal of Power Sources*. 1995;54:76-84.
- [55] Sloop SE, Kerr JB, Kinoshita K. The role of Li-ion battery electrolyte reactivity in performance decline and self-discharge. *Journal of Power Sources*. 2003;119-121:330-7.
- [56] Yoshida H, Fukunaga T, Hazama T, Terasaki M, Mizutani M, Yamachi M. Degradation mechanism of alkyl carbonate solvents used in lithium-ion cells during initial charging. *Journal of Power Sources*. 1997;68:311-5.
- [57] Shin J-S, Han C-H, Jung U-H, Lee S-I, Kim H-J, Kim K. Effect of  $\text{Li}_2\text{CO}_3$  additive on gas generation in lithium-ion batteries. *Journal of Power Sources*. 2002;109:47-52.
- [58] Kumai K, Miyashiro H, Kobayashi Y, Takei K, Ishikawa R. Gas generation mechanism due to electrolyte decomposition in commercial lithium-ion cell. *Journal of Power Sources*. 1999;81-82:715-9.
- [59] Richard MN, Dahn JR. Accelerating Rate Calorimetry Study on the Thermal Stability of Lithium Intercalated Graphite in Electrolyte. I. Experimental. *Journal of The Electrochemical Society*. 1999;146:2068-77.
- [60] Bak S-M, Nam K-W, Chang W, Yu X, Hu E, Hwang S, et al. Correlating Structural Changes and Gas Evolution during the Thermal Decomposition of Charged  $\text{Li}_{x}\text{Ni0.8Co0.15Al0.05O}_2$  Cathode Materials.

Chemistry of Materials. 2013;25:337-51.

- [61] Nam K-W, Bak S-M, Hu E, Yu X, Zhou Y, Wang X, et al. Combining In Situ Synchrotron X-Ray Diffraction and Absorption Techniques with Transmission Electron Microscopy to Study the Origin of Thermal Instability in Overcharged Cathode Materials for Lithium-Ion Batteries. Advanced Functional Materials. 2013;23:1047-63.
- [62] Birch A, Brown D, Dodson M, Swaffield F. The Structure and Concentration Decay of High Pressure Jets of Nature Gas. COMBUSTION SCIENCE AND TECHNOLOGY. 1984;36:249-61.
- [63] Birch AD, Hughes DJ, Swaffield F. Velocity Decay of High Pressure Jets. Combustion Science and Technology. 1987;52:161-71.
- [64] Cumber PS. Predicting Outflow from High Pressure Vessels. Process Safety and Environmental Protection. 2001;79:13-22.
- [65] Duan Z, Ding G, Tang W, Ren T. A thermodynamic model for predicting transient pressure evolution in response to venting and vaporization of liquefied gas under sudden release. Journal of Hazardous Materials. 2020;395:122460.
- [66] Zhou Y, Wu J, Lemmon EW. Thermodynamic Properties of Dimethyl Carbonate. Journal of Physical and Chemical Reference Data. 2011;40:043106.
- [67] Argyropoulos CD, Markatos NC. Recent advances on the numerical modelling of turbulent flows. Applied Mathematical Modelling. 2015;39:693-732.
- [68] Launder BE, Sharma BI. Application of the energy-dissipation model of turbulence to the calculation of flow near a spinning disc. Letters in Heat and Mass Transfer. 1974;1:131-7.
- [69] Chen S, Wang Z, Yan W. Identification and characteristic analysis of powder ejected from a lithium ion battery during thermal runaway at elevated temperatures. Journal of Hazardous Materials. 2020;400:123169.
- [70] Magnussen B. On the structure of turbulence and a generalized eddy dissipation concept for chemical reaction in turbulent flow. 19th Aerospace Sciences Meeting: American Institute of Aeronautics and Astronautics; 1981.
- [71] Maragkos G, Beji T, Merci B. Advances in modelling in CFD simulations of turbulent gaseous pool fires. Combustion and Flame. 2017;181:22-38.
- [72] McBride B, Gordon S, Reno M. Coefficients for calculating thermodynamic and transport properties of individual species. NASA Technical Memorandum 4513. 1993.
- [73] Sutherland W. The Viscosity of Gases and Molecular Force. The London. 1893;Edinburgh:507-31.
- [74] Poling B, Prausnitz J, O'Connell J. The Properties of Gases and Liquids2000.
- [75] Otsu N. A Threshold Selection Method from Gray-Level Histograms. IEEE Transactions on Systems, Man, and Cybernetics. 1979;9:62-6.
- [76] Incropera F. Fundamentals of Heat and Mass Transfer. New York: Wiley. 1985.
- [77] Zou K, Chen X, Ding Z, Gu J, Lu S. Jet behavior of prismatic lithium-ion batteries during thermal runaway. Applied Thermal Engineering. 2020;179:115745.
- [78] Chen H, Buston JEH, Gill J, Howard D, Williams RCE, Rao Vendra CM, et al. An experimental study on thermal runaway characteristics of lithium-ion batteries with high specific energy and prediction of heat release rate. Journal of Power Sources. 2020;472:228585.